CHALMERS

LARGE EDDY SIMULATION OF THE FLOW AROUND A HIGH-LIFT AIRFOIL

SIMON DAHLSTRÖM

Department of Thermo and Fluid Dynamics
CHALMERS UNIVERSITY OF TECHNOLOGY
Göteborg Sweden, 2000

THESIS FOR THE DEGREE OF LICENTIATE IN ENGINEERING

LARGE EDDY SIMULATION OF THE FLOW AROUND A HIGH-LIFT AIRFOIL

SIMON DAHLSTRÖM

Department of Thermo and Fluid Dynamics
CHALMERS UNIVERSITY OF TECHNOLOGY
Göteborg Sweden, 2000

LARGE EDDY SIMULATION OF THE FLOW AROUND A HIGH-LIFT AIRFOIL

Simon Dahlström

Department of Thermo and Fluid Dynamics
Chalmers University of Technology
SE-412 96 Göteborg, Sweden
e-mail: sd@tfd.chalmers.se
webpage: http://www.tfd.chalmers.se/~sd/project.html

Abstract

The work presented in this thesis is part of the ongoing Brite-Euram project, LESFOIL. In the project, Large Eddy Simulation (LES) is used to calculate the flow around the Aerospatiale A-profile at an angle of attack of 13.3° and a chord Reynolds number of $2.1 \cdot 10^6$.

The method used is an incompressible implicit second-order finite volume method with a collocated grid arrangement. To suppress unphysical oscillations (mainly generated from the leading edge area), upwinding is used in front of the airfoil and upstream of the transition point. In the transition region, the scheme is gradually mixed with the central difference scheme (CDS). The non-dissipative CDS gives rise to numerical oscillations and the boundary layer is tripped numerically. Although the transition is unnatural, the unphysical oscillations are dampened in the area downstream of the transition.

The requirements on the resolution, for this particular case, are investigated. A wall-resolved LES is too expensive and approximate wall boundary conditions are used. None of the present computations predict trailing edge separation. However, before any conclusions are drawn about the feasibility of LES for this case, the coarse resolution in the laminar boundary layer and the unnatural transition must be treated.

Keywords: Large Eddy Simulation, Incompressible Finite Volume, Airfoil, Transition, Separation, Approximate Wall Boundary Condition, Upwinding.

Contents

Acknowledgements

This work was carried out at the Department of Thermo and Fluid Dynamics at Chalmers University of Technology. The LESFOIL project, (Project No. BRPR-CT97-0565) is financed by the Brite-Euram programme.

I would really like to express my gratitude to my supervisor Prof. Lars Davidson, who has been an encouraging support. I would also like to express my gratitude to all of my colleagues in the LESFOIL project and to all at our department.

Preface

This thesis is primarily based on the work reported in Chapter 4, which will appear (in the following paper) as:

S. Dahlström and L. Davidson, Large Eddy Simulation of the Flow around an Aerospatiale A-Aerofoil, ECCOMAS 2000, European Congress on Computational Methods in Applied Sciences and Engineering, Barcelona, Spain, 11-14 Septemper, 2000.

1 Introduction

The LESFOIL project investigates the feasibility of Large Eddy Simulations (LES) of flows around simple 2D airfoils (see [1], where the project is presented). The airfoil case chosen is the flow around the Aerospatiale A-airfoil at an angle of attack, α, of 13.3°. The chord Reynolds number is $2.1 \cdot 10^6$ and the flow is subsonic with a freestream Mach number of 0.15. These are high-lift conditions at take-off and landing.

The flow around the Aerospatiale A-airfoil has been the subject of extensive study. Different CFD codes (steady and unsteady RANS, compressible and incompressible methods) were validated in the EUROVAL project [2] and in the ECARP project [3] on this particular single-element airfoil. It was found that few RANS models are capable of handling this flow problem, mainly because of the lack of curvature effects in the eddy-viscosity models. The second-moment closures (which do take into account curvature effects) produced the best results, see also Refs. [4, 5, 6]. Much because of the rate at which computer power is increasing, LES is becoming an interesting approach applicable for more complex flows.

This is a challenging case for LES owing to the high Reynolds number and because of the different flow regimes around the airfoil, which are sketched in Fig. 1. At the leading edge there is a very thin laminar boundary layer. On the pressure side, this boundary layer is tripped at 30% of the chord and there is a transition to a very thin turbulent boundary layer. On the suction side, there is a peak in the pressure gradient near the leading edge. The favorable pressure gradient accelerates the flow around the leading edge. In this case the flow separates, a separation bubble is formed and, when the flow reattaches at about 12% of the chord, the boundary layer becomes turbulent. The boundary layer grows under the influence of an adverse pressure gradient and, at about 82.5% of the chord, the flow separates. In the wake, downstream of the trailing edge, the low-speed flow from the separation region on the suction side forms a mixed shear layer with the flow from the very

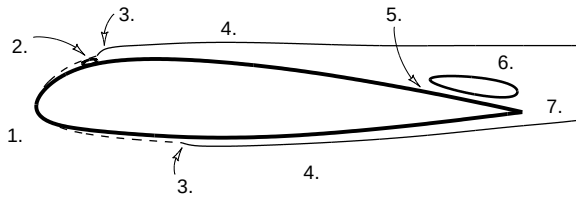

Figure 1: Schematic sketch of the flow regimes around the Aerospatiale A-profile: 1. laminar boundary layer, 2. laminar separation bubble, 3. transition region, 4. turbulent boundary layer, 5. separation point, 6. separation region, 7. wake region.

thin boundary layer on the pressure side.

Even at the from an aeronautical point of view low Reynolds number, a wall-resolved LES is too expensive. The use of approximate boundary conditions in the near-wall region is necessary, and a good method of prescribing and controlling the transition is needed. Still, the requirements on the mesh are demanding and result in meshes with a large number of nodes. For this reason, an efficient numerical method with an effective parallelization is needed.

Results from four computations on two meshes are presented, with focus on the last three, where upwinding is used in part of the domain to prescribe the transition and suppress unphysical oscillations. The outline of this thesis is the following. The next chapter summarises some LES theories and the following chapter describes the numerical method. Chapters 4 and 5 present the airfoil case and computations, where Chapter 4 includes the ECCOMAS paper [7] and additional results are presented in Chapter 5. Finally, the last chapter presents some spectral analysis theory and applications.

2 Large Eddy Simulation

This chapter deals with the basic ideas of Large Eddy Simulation (LES). Smagorinsky (1963) presented the first subgrid scale (SGS) model, and it is his model, perhaps the simplest, that is considered in this thesis. It should be mentioned that a range of SGS models has been developed since 1963, one of the outstanding contributions being that of Germano *et al.* [8], who introduced the dynamic approach in SGS modeling. This model and some other dynamic models are presented in e.g. [9].

2.1 Mathematical Formulation

In LES, the large eddies are solved and the small scales are modeled. Mathematically, you filter the governing equations by applying the *filter operator*, G, to the equations. The filter operator is defined as:

$$Gf \equiv \overline{f} = \int G(\mathbf{x}, \mathbf{x}', \Delta(\mathbf{x})) f(\mathbf{x}') d\mathbf{x}'$$

where $G(\mathbf{x}, \mathbf{x}', \Delta(\mathbf{x}))$ is the *filter function* and Δ is the *filter width*. An example of a filter function (used in the present work) is the box filter, defined in one dimension as

$$G(x, x') = \begin{cases} 1/\Delta & , \; x - \Delta/2 < x' < x + \Delta/2 \\ 0 & , \; \text{otherwise} \end{cases} . \tag{1}$$

Filtering of the incompressible continuity and momentum equations results in

$$\frac{\partial \overline{u}_i}{\partial x_i} = 0 \tag{2}$$

$$\frac{\partial \overline{u}_i}{\partial t} + \frac{\partial}{\partial x_j}(\overline{u}_i \overline{u}_j) = -\frac{1}{\rho}\frac{\partial \overline{p}}{\partial x_i} + \frac{\partial}{\partial x_j}\left[\nu \frac{\partial \overline{u}_i}{\partial x_j} - \tau_{ij}\right] \tag{3}$$

where

$$\tau_{ij} = \overline{u_i u_j} - \overline{u}_i \overline{u}_j \tag{4}$$

are the subgrid stresses, which are unknown and must be modeled.

In this derivation of the filtered equations, it has been assumed that the filter operator commutes with the spatial derivatives. This is not true for all filter functions, $G(\mathbf{x}, \mathbf{x}', \Delta(\mathbf{x}))$ (as pointed out in e.g. [9]), because, in one dimension, the following integral identity is valid:

$$\int \frac{\partial f(x')}{\partial x'} G(x, x', \Delta(x)) dx' = \frac{d}{dx}\int f(x') G(x, x', \Delta(x)) dx' +$$

$$\int -f(x') \left[\frac{\partial}{\partial x'} G(x, x', \Delta(x)) + \frac{\partial}{\partial x} G(x, x', \Delta(x))\right] dx'$$

i.e. $GDf = DGf + R$, where R is the commutation error and D is the spatial derivative operator. It is clearly seen that the commutation error is zero for those functions that satisfy the following condition:

$$\frac{\partial}{\partial x'} G(x, x', \Delta(x)) = -\frac{\partial}{\partial x} G(x, x', \Delta(x)) \tag{5}$$

The functions that satisfy this condition are of the convolution type, $G(x, x', \Delta(x)) = G(x - x', \Delta(x) = \text{constant})$, i.e. they depend only on $x - x'$. Note also that $\Delta(x)$ must be constant.

The filter width, Δ, is often the same as the grid size. To keep the number of computational nodes at a minimum, the grid is often refined in the regions of interest, e.g. close to a wall or in a shear layer. This leads to a commutation error in most computations, since then $\partial\Delta/\partial x \neq 0$.

2.2 Smagorinsky Subgrid Scale Model

The subgrid scale stresses (4) are the contribution of the small scales, the unresolved stresses. They are unknown and must be modeled. The scales are of the order of the filter width, Δ, and, by using the Eddy viscosity assumption and mixing length theory, the anisotropic part of τ_{ij} is modeled, according to Smagorinsky (1963), as:

$$\begin{aligned} &\tau_{ij} - \tfrac{1}{3}\delta_{ij}\tau_{kk} = -2\nu_T \overline{S}_{ij} \quad , \quad \nu_T = (C_S\Delta)^2 |\overline{S}| \\ &\text{and} \quad |\overline{S}| = \sqrt{2\overline{S}_{ij}\overline{S}_{ij}} \end{aligned} \tag{6}$$

Here, $\overline{S}_{ij} = \frac{1}{2}\left(\frac{\partial \overline{u}_i}{dx_j} + \frac{\partial \overline{u}_j}{dx_i}\right)$ is the filtered strain rate and ν_T is the Smagorinsky eddy viscosity.

Since the Smagorinsky model is an *algebraic* eddy viscosity model, there is an assumption of isotropy for the unresolved scales, which means that the turbulence is in local equilibrium. The SGS kinetic energy equation then reads

$$-\tau_{ij}\overline{S}_{ij} = \text{dissipation} \, , \tag{7}$$

where the production term, $-\tau_{ij}\overline{S}_{ij}$, acts as a dissipation term in the resolved kinetic energy equation (see [10]). This illustrates the main task of an SGS model: to dissipate the correct amount of energy from the resolved scales acting through the *subgrid scale dissipation*, $\varepsilon_{sgs} = \tau_{ij}\overline{S}_{ij}$.

2.3 Local Isotropy

The assumption that the smallest scales are isotropic is in accordance with Kolmogorov's (1941) universal equilibrium theory, which states

that if the Reynolds number is high enough then there exists a range of wave numbers, the *equilibrium range*, where the scales are independent of the large scale flow and depend only on the dissipation rate, ϵ, and the viscosity, ν. Not only this theory but also the existence of an *inertial subrange* (where the eddies are also independent of the viscosity) have been confirmed in experiments and simulations. The Kolmogorov theory implies *local isotropy* for the smallest scales, for which the time scales are much smaller than for the larger scales, and the small scales lose any sense of direction given by an anisotropic large scale flow (Tennekes and Lumley [11])). For example, Saddoughi and Veeravalli [12] have found clear indications of local isotropy in the inertial subrange in their measurements in a high Reynolds turbulent boundary layer flow.

In LES, assuming that the inertial range dynamics (and the local isotropy) sets in independently of the Reynolds number relative to the largest scale in the flow, ℓ, then the required resolution in an LES is also independent of the Reynolds number. This in contrast to DNS (Direct Numerical Simulation), where almost all scales in a flow field are resolved, from the largest scales down to the Kolmogorov length scales. The Kolmogorov scales are the smallest scales in a turbulent flow, with the length scale, η, time scale, τ, and the velocity scale, v, given by:

$$\eta \equiv \left(\nu^3/\varepsilon\right)^{1/4} \quad \tau \equiv (\nu/\varepsilon)^{1/2} \quad v \equiv (\nu\varepsilon)^{1/4} \tag{8}$$

The structure of the turbulence becomes finer as the Reynolds number ($Re_\ell = u\ell/\nu$) increases. Thus the DNS resolution has to increase with increasing Reynolds number. If the largest scales in a flow are of the size ℓ, the number of nodes required in a DNS, in one direction, is proportional to ℓ/η ($\sim Re_\ell^{3/4}$). The total number of nodes thus scales like $Re_\ell^{9/4}$, and the numerical problem becomes unsolvable at a relatively low Reynolds number.

2.4 Near-Wall Problem of LES

The LES idea seems to work well in the case of turbulence with inertial range dynamics (wake flows, jets and outer boundary layers at high Reynolds numbers). The inertial subrange decreases approaching a solid boundary, however, and local isotropy is found only at smaller and smaller scales. Saddoughi and Veeravalli [12] have suggested that the criterion for local isotropy, in simple shear flows, scales with the strain rate, S. The strain rate of course becomes larger the closer to the wall, indicating the increase in anisotropy at smaller scales the closer we come to a solid boundary. Also, very close to the wall, the important *near wall streaks* must be sufficiently resolved. These coherent structures in the viscous sublayer are important since they interact with the

buffer region and are responsible for a major part of the energy production in this region [13].

It has been estimated that using LES around an airplane wing at a chord Reynolds number of 10^7 would require a number of nodes in the order of 10^{11} [14]. This clearly illustrates the near-wall problem of LES. There is definitely a need for approximate wall boundary conditions in high Reynolds simulations, such as prescribing a wall law. Either approximate wall boundary conditions or a different approach may be used, for example the Detached Eddy Simulation (DES) approach, using Reynold's Averaged Navier Stokes (RANS) near walls and LES in the detached part of the flow (see e.g. [14, 15]).

3 Numerical Method

The code used is an incompressible finite volume Navier-Stokes solver called CALC-BFC (Davidson and Farhanieh [16]). The solver is based on structured grids and the use of curvi-linear boundary fitted coordinates. The grid arrangement is collocated, and the Rhie and Chow interpolation method [17] is used. The code is parallelised for 3D flows [18] using block decomposition and the message passing systems PVM and MPI. See Section 4.7 in the next chapter for a more detailed analysis of the efficiency of the parallelisation as well as some notes on the convergence criteria. The PISO algorithm is used for the pressure-velocity coupling, and is described in more detail in Section 3.3. The PISO algorithm was chosen over a version of the SIMPLEC algorithm because it performed better in a simple test case, the flow over a backward facing step (see Section 3.5).

The mathematical formulation of Large Eddy Simulation (LES) was described in the previous chapter. The filtered momentum equations (Eqs. 3) are discretised in time using the Crank-Nicolson scheme and in space using 2nd order difference schemes (the central difference scheme (CDS) and the van Leer scheme). The CDS is often used in LES because of its non-dissipative and energy-conserving properties. Section 3.2 addresses the motivation for using a dissipative upwind scheme (as the van Leer scheme) in certain parts of the computational domain. As a subgrid scale model, the Smagorinsky model (see Eq. 6) is used with the Smagorinsky constant, C_S, equal to 0.1. In the present work, the crossterm, $\nu_T \partial \overline{u}_j / \partial x_i$, has been omitted. No *explicit* filtering is used. The filter width, Δ, is computed using the definition $\Delta^3 = \Delta x \Delta y \Delta z = \delta V$, i.e. Δ is taken as the cubic root of the volume of a finite volume cell (*implicit* filtering).

The discretised momentum equations are solved with the CGSTAB solver and the SIP solver is used for the discretised pressure correction equation. The rate of convergence for iterative solvers depends on the discretisation. Two alternative ways of implementing a spatial scheme are described in Section 3.1 and compared in a numerical test case, the flow over a backward facing step (see Section 3.5).

3.1 Implementation of the Spatial Schemes

When central difference approximations are used for the convective fluxes in the momentum equations, the equation systems may not be diagonally dominant, leading to no convergence for most iterative solvers. The discretisation of the filtered momentum equations for velocity component u_i (the bar denoting filtering is dropped for convenience) results

in an equation system

$$a_p u_{i,p}^m = \sum_{nb} a_{nb} u_{i,nb}^m + Q \ , \tag{9}$$

where the subscript nb refers to the neighbouring nodes, Q is the right-hand side (containing e.g. the pressure gradient) and the superscript m denotes the present outer iteration. A sufficient condition for a converging iterative method, applied to the equation system above, is

$$\frac{\sum_{nb} |a_{nb}|}{|a_p|} \begin{cases} \leq 1 \text{ at all nodes} \\ < 1 \text{ at one node at least} \end{cases} , \tag{10}$$

which is called the Scarborough criterion. This is equivalent to the resulting matrix being positive semi definite or diagonally dominant. This is not the case for central difference schemes at high Peclet numbers ($Pe = u\Delta x/\nu > 2$ for 2nd order CDS). Some coefficients might be negative, which results in a very ill conditioned equation system with very small diagonal coefficients.

One way of improving the ill conditioned equation system was presented by Davidson & Hellström [19], who modified the equation system above (Eq. 9) by adding

$$\sum_{nb} (|a_{nb}| - a_{nb}) \tag{11}$$

to the diagonal coefficients a_p and

$$u_{i,p}^{m-1} \sum_{nb} (|a_{nb}| - a_{nb}) \tag{12}$$

to the right-hand side Q, where $u_{i,p}^{m-1}$ are the velocities from the previous outer iteration ($m-1$). In this way, the equation system is more well conditioned and the rate of convergence is increased. Especially, it now fulfills the Scarborough criterion.

Another way of reassuring that the Scarborough criterion is satisfied is by using a first order upwind scheme in the coefficients a_p and a_{nb}. This is the idea in the *deferred correction* approach (see Ferziger and Perić [20]). Deferred correction implies that the convective flux may be expressed as

$$\dot{m} u_{UDS}^m + \dot{m} (u_{CDS}^{m-1} - u_{UDS}^{m-1}) \ , \tag{13}$$

where CDS stands for the higher (2nd) order central difference scheme and UDS for the lower (1st) order upwind scheme.

Provided that the equation system converges, these approaches lead to the same accuracy as that of the central difference scheme (and also to the same solution). The difference is that we are able to *get* a solution and at a higher rate of convergence.

3.2 Mixed Schemes

The approaches described in the previous section increase the rate of convergence for the iterative solvers (and the method in total), but the solution is of course still the 'CDS solution' (if the number of outer iterations are sufficient) and contains the good as well as the bad properties of that scheme. As mentioned above, the central difference approximations are often used in LES because of its non-dissipative and energy-conserving properties. However, central difference schemes are also known to produce *odd-even* oscillations (*grid-to-grid* oscillations or *wiggles*) when the resolution is poor. Sources of these wiggles in high Reynolds number simulations can be the outflow boundary condition and high cell Peclet numbers ($Pe = u\Delta x/\nu$) in *combination* with large streamwise gradients of the advected variable [21]. To remove such unphysical wiggles in regions where the above conditions are particularly severe, e.g. in front of an airfoil, 2nd-order upwinding might be used in part of the domain. The scheme used is blended, so that the convective flux can be expressed as:

$$\dot{m}u^m_{UDS} + \dot{m}\left[\alpha u^{m-1}_{CDS} - \alpha u^{m-1}_{UDS} + (1-\alpha)u^{m-1}_{UDScorr}\right] \quad , \tag{14}$$

where CDS stands for the central difference scheme, UDS for the lower order upwind scheme and $UDScorr$ for the 2nd-order correction to the 1st-order upwind scheme. As before, $m-1$ is the previous outer iteration and here α is a blending function ($0 \leq \alpha \leq 1$). At the extremes we have:

$\alpha = 0$: the van Leer scheme
$\alpha = 1$: the central difference scheme with deferred correction

A value of α closer to zero could then be used in regions where the odd-even oscillations are too severe.

3.3 The PISO Algorithm

The PISO algorithm was presented by Issa [22], and the algorithm is described for staggered grid arrangement in [20] and [23]. It should be noted that, in this section, the algorithm is described in the way in which it is implemented in our collocated code.

The previous sections discussed the solution of the discretised momentum equations. The discretised momentum equations are solved with an iterative method as described above. The pressure from the previous iteration, p^{m-1}, is used when solving these equations and, if the solutions to these equations are denoted with $u^{m*}_{i,p}$, the equation systems may be written

$$a_p u^{m*}_{i,p} = \sum_{nb} a_{nb} u^{m*}_{i,nb} + Q^{m-1}_{u_i} - \frac{1}{2}\left(\frac{\partial p^{m-1}}{\partial x_i}\right)_p \delta V \ . \tag{15}$$

Here the last term, the implicit pressure gradient term, has been taken out of the right-hand side, Q, as compared with Eq. 9. This is because we are interested here in solving for the pressure, i.e. we focus on the pressure-velocity coupling. Note also that the factor $1/2$ arising from the Cranc-Nicolson method is 'hidden' in the coefficients and the right-hand side, Q. In the above equations, the velocities do not necessarily satisfy the continuity equation. If we denote those velocities and the pressure that satisfy both the discretised momentum equations *and* the continuity equation by u_i and p, these equation systems can be written as (for simplicity we drop $1/2$ in front of $\partial p/\partial x$ in Eq. 15)

$$a_p u_{i,p} = \sum_{nb} a_{nb} u_{i,nb} + Q_{u_i}^{m-1} - \left(\frac{\partial p}{\partial x_i}\right)_p \delta V \ . \tag{16}$$

The idea in the PISO algorithm is to obtain these velocities (u_i) and the pressure (p) in an iterative algorithm. Of course, it is of little use to converge such an algorithm, since the coefficients and the right-hand side contain the velocities from the previous iteration. Nevertheless, it may be more efficient than the basic version, the SIMPLE algorithm.

First corrector step (SIMPLE algorithm)

Introducing the velocity corrections, $u'_{i,p}$,

$$u_{i,p} = u_{i,p}^{m*} + u'_{i,p} \tag{17}$$

and the pressure correction, p',

$$p = p^{m-1} + p' \ , \tag{18}$$

the relation between the corrections is obtained by subtracting Eq. 15 from Eq. 16:

$$u'_{i,p} = \tilde{u}'_{i,p} - \frac{1}{a_p}\left(\frac{\partial p'}{\partial x_i}\right)_p \delta V \ , \text{ where } \quad \tilde{u}'_{i,p} = \frac{\sum_{nb} a_{nb} u'_{i,nb}}{a_p} \ . \tag{19}$$

Now, the continuity equation, $\partial(\rho u_i)/\partial x_i = 0$, together with Eqs. 17 and 19, produce a pressure correction equation:

$$\frac{\partial}{\partial x_i}\left[\frac{\rho}{a_p}\frac{\partial p'}{\partial x_i}\delta V\right]_p = \left[\frac{\partial(\rho u_i^{m*})}{\partial x_i}\right]_p + \left[\frac{\partial(\rho \tilde{u}'_i)}{\partial x_i}\right]_p \ . \tag{20}$$

The pressure-velocity coupling can give rise to non-physical oscillations in the pressure and velocity fields when non-staggered grids are used. To avoid this problem, the velocities, when evaluated on the faces of the cells, are interpolated using the Rhie and Chow method [17]. As u' is unknown, $\tilde{u}'$ is neglected in the equation above (Eq. 20) and a Rhie

and Chow velocity $u_i^{R.C.}$ is instead added to u_i^{m*}. The *modified* pressure correction equation then becomes:

$$\frac{\partial}{\partial x_i}\left[\frac{\rho}{a_p}\frac{\partial p'^*}{\partial x_i}\delta V\right]_p = \left[\frac{\partial(\rho u_i^{m*})}{\partial x_i}\right]_p + \left[\frac{\partial(\rho u_i^{R.C.})}{\partial x_i}\right]_p . \tag{21}$$

This equation is solved for the *approximate* pressure correction, p'^*, and the *approximate* velocity correction, u'^*, is obtained (from Eq. 19 with $\tilde{u}'$ neglected) as:

$$u_{i,p}'^* = -\frac{1}{a_p}\left(\frac{\partial p'^*}{\partial x_i}\right)_p \delta V . \tag{22}$$

This is the first step in the PISO algorithm as it is implemented in our code, and this corresponds to the SIMPLE algorithm.

Second corrector step

Similarly, in the second corrector step, the correct solutions are now decomposed as

$$u_{i,p} = u_{i,p}^{m*} + u_{i,p}'^* + u_{i,p}'' \tag{23}$$

and

$$p = p^{m-1} + p'^* + p'' . \tag{24}$$

The relation between the new corrections are obtained by using Eq. 19 (i.e. subtraction of Eq. 15 from Eq. 16):

$$u_{i,p}'' = \tilde{u}_{i,p}'^* + \tilde{u}_{i,p}'' - \frac{1}{a_p}\left(\frac{\partial p''}{\partial x_i}\right)_p \delta V \ , \text{ where} \tag{25}$$
$$\tilde{u}_{i,p}'^* = \frac{\sum_{nb} a_{nb} u_{i,nb}'^*}{a_p} \quad \text{and} \quad \tilde{u}_{i,p}'' = \frac{\sum_{nb} a_{nb} u_{i,nb}''}{a_p} .$$

Now, putting Eq. 23 in the continuity equation and using Eq. 25 and Eq. 21, the second pressure correction equation becomes

$$\frac{\partial}{\partial x_i}\left[\frac{\rho}{a_p}\frac{\partial p''}{\partial x_i}\delta V\right]_p = \left[\frac{\partial(\rho\tilde{u}_i'')}{\partial x_i}\right]_p + \left[\frac{\partial(\rho\tilde{u}_i'^*)}{\partial x_i}\right]_p - \left[\frac{\partial(\rho u_i^{R.C.})}{\partial x_i}\right]_p , \tag{26}$$

where here also Eq. 22 has been used. As before, in order to smooth out the pressure correction, a Rhie and Chow velocity gradient term is added to the right-hand side and, also, since $u_{i,p}''$ is unknown, $\tilde{u}_i''$ is neglected in the equation above. This results in the modified pressure correction equation:

$$\frac{\partial}{\partial x_i}\left[\frac{\rho}{a_p}\frac{\partial p''^*}{\partial x_i}\right]_p = \left[\frac{\partial(\rho\tilde{u}_i'^*)}{\partial x_i}\right]_p . \tag{27}$$

The equation for the modified pressure correction, p''^*, is solved and new values of the velocity corrections, $u''^*_{i,p}$, are obtained (by neglecting $\tilde{u}''_i$ in Eq.25) as

$$u''^*_{i,p} = \tilde{u}'^*_{i,p} - \frac{1}{a_p}\left(\frac{\partial p''}{\partial x_i}\right)_p \delta V \ , \text{ where} \qquad (28)$$

$$\tilde{u}'^*_{i,p} = \frac{\sum_{nb} a_{nb} u'^*_{i,nb}}{a_p}$$

This, the second corrector step, can be repeated more times in a similar manner. Finally, the new values, at the present iteration, $u^m_{i,p}$ and p^m, are obtained as $u^m_{i,p} = u^{m*}_{i,p} + u'^*_{i,p} + u''^*_{i,p} + \ldots$ and $p^m = p^{m-1} + p'^* + p''^* + \ldots$.

3.4 The SIMPLEC Algorithm

The SIMPLEC algorithm consists of only one step. Just as in the SIMPLE algorithm (the first step in the PISO algorithm), the velocity and pressure corrections are defined (Eq. 17 and 18), and the relation between the corrections is obtained as

$$u'_{i,p} = \tilde{u}'_{i,p} - \frac{1}{a_p}\left(\frac{\partial p'}{\partial x_i}\right)_p \delta V \ , \text{ where} \quad \tilde{u}'_{i,p} = \frac{\sum_{nb} a_{nb} u'_{i,nb}}{a_p} \ . \qquad (29)$$

Instead of neglecting the first term on the right-hand side, $\tilde{u}'_{i,p}$, it can be estimated. In the SIMPLEC algorithm, the velocity corrections in the neighbouring nodes are estimated as the corrections in node p:

$$\tilde{u}'_{i,p} = \frac{\sum_{nb} a_{nb} u'_{i,nb}}{a_p} \approx u'_{i,p} \frac{\sum_{nb} a_{nb}}{a_p} \qquad (30)$$

and Eq. 29 can then be written

$$u'_{i,p} = \frac{-1}{a_p - \sum_{nb} a_{nb}} \left(\frac{\partial p'}{\partial x_i}\right)_p \delta V \ . \qquad (31)$$

Note that the under-relaxation factor, α, and the coefficient, a^0, arising from the time discretisation, is included in a_p, i.e. $a_p = \alpha^{-1}(\sum_{nb} a_{nb} + a^0)$. Now, the continuity equation, $\partial(\rho u_i)/\partial x_i = 0$, together with Eq. 17 and the above relation, produce a modified pressure correction equation:

$$\frac{\partial}{\partial x_i}\left[\frac{\rho}{a_p - \sum_{nb} a_{nb}} \frac{\partial p'^*}{\partial x_i} \delta V\right]_p = \left[\frac{\partial(\rho u_i^{m*})}{\partial x_i}\right]_p + \left[\frac{\partial(\rho u_i^{R.C.})}{\partial x_i}\right]_p \qquad (32)$$

where the Rhie and Show contribution has also been added. This equation is solved for the *approximate* pressure correction, p'^*, giving the new pressure $p^m = p^{m-1} + p'^*$ and the new velocities $u^m_{i,p} = u^{m*}_{i,p} + u'^*_{i,p}$, where the velocity corrections, $u'^*_{i,p}$, are obtained from Eq. 31, as

$$u'^*_{i,p} = \frac{-1}{a_p - \sum_{nb} a_{nb}} \left(\frac{\partial p'^*}{\partial x_i}\right)_p \delta V \ . \qquad (33)$$

3.5 Numerical Test Case: Backward Facing Step

The flow over a backward facing step is used as a test case. The step is large ($2.5h$, where h is the inlet height). Two different meshes have been used, one coarse ($130 \times 82 \times 42$ nodes) and one finer ($130 \times 82 \times 82$ nodes). The width of the computational domain is $18h$, and the extension downstream the step is $69h$.

The flow at a Reynolds number of 5000 (based on the inlet velocity and inlet height) is computed using LES with the Smagorinsky subgrid model ($C_S = 0.1$). For the advancement in time, the Crank-Nicolson scheme is used, except for the pressure, which *here* is treated in a fully implicit way. A $1/7$ profile is used as inlet data and a convective boundary condition, $\partial\phi/\partial t + U_c\partial\phi/\partial x = 0$, is used at the outlet. The no-slip condition is used at all walls. The time step is set to 0.26 seconds, which gives a maximum CFL number smaller than 1.2.

3.5.1 Speed-up

A $k-\varepsilon$ solution is taken as an initial solution for the LES. The effectiveness of the message passing PVM code was tested using the k-ε model on the finer mesh. With the domain divided into one, four and eight sub domains, the speed-up (measured in time elapsed until convergence is reached) was found to be 4.3 and 8.3 on four and eight processors, respectively. Here the momentum equations were discretised using the hybrid difference scheme. In this simple case, the speed-up is approximately linear.

3.5.2 Deferred correction

LES computations on the coarse mesh when using the SIMPLEC algorithm for the pressure-velocity coupling resulted in a higher rate of convergence when the deferred correction approach was used. Here the stationary version of SIMPLEC has been used, i.e. $\tilde{u}'_{i,p}$ in Eq. 30 has been estimated as $u'_{i,p}\alpha$, which is a reasonable approximation, only if $a^0/\sum_{nb} a_{nb}$ is small. For various under-relaxation parameters for the velocities, the number of iterations per time step decreased by approximately 10% (see Fig. 2). Eight processors were used in these computations.

3.5.3 PISO and SIMPLEC

In the computations with eight processors on the coarse grid, the number of iterations per time step was found to be approximately 5.4 with the PISO algorithm. Although the PISO algorithm is more time consuming per iteration than the SIMPLEC algorithm (in this case approx-

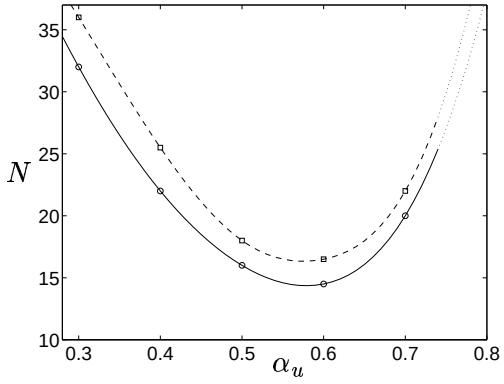

Figure 2: Number of iterations, N, per time step versus the under-relaxation parameter for the velocities α_u ($= \alpha_v = \alpha_w$; $\alpha_{p'} = 1$). Circles: the deferred correction approach; squares: the modification in Ref. [19].

imately 30% more expensive), the time per time step for the PISO algorithm (with no under-relaxation) was reduced by approximately 50% compared with the *optimized* SIMPLEC algorithm ($\alpha_u = 0.6$ in Fig. 2). There was just one inner iteration in the second corrector step in these computations. Further evaluation can be done in optimizing the PISO algorithm.

4 Large Eddy Simulation of the Flow around an Aerospatiale A-Aerofoil

This chapter will appear as

S. Dahlström and L. Davidson, Large Eddy Simulation of the Flow around an Aerospatiale A-Aerofoil, ECCOMAS 2000, European Congress on Computational Methods in Applied Sciences and Engineering, Barcelona, Spain, 11-14 Septemper, 2000.

abstract

The work presented in this paper is part of the ongoing Brite-Euram project LESFOIL. In the project, Large Eddy Simulation (LES) is used to calculate the flow around the Aerospatiale A-profile at an angle of attack of 13.3° *and a chord Reynolds number of* $2.1 \cdot 10^6$.

The method used is an incompressible implicit second-order finite volume method with a collocated grid arrangement. To suppress unphysical oscillations (mainly generated from the leading edge area), upwinding is used in front of the airfoil and upstream of the transition point. In the transition region, the scheme is gradually mixed with the central difference scheme (CDS). The non-dissipative CDS gives rise to numerical oscillations and the boundary layer is tripped numerically. Although the transition is unnatural, the unphysical oscillations are dampened in the area downstream of the transition.

Four simulations have been carried out, one using an approximate wall boundary condition and the other three using the no-slip condition. None of the present computations predict separation. However, the importance of the spanwise resolution is demonstrated in these attached boundary layer simulations. Before any conclusions are drawn about the feasibility of LES for this case, the number of nodes in the wall-normal direction must be increased or some other approach has to be applied in order to treat the coarse resolution in the laminar boundary layer.

4.1 Introduction

The feasibility of Large Eddy Simulations (LES) of flows around simple, 2D airfoils is investigated in the LESFOIL project (see [1], where the project is presented). The airfoil case chosen is the flow around the Aerospatiale A-airfoil at an angle of attack, α, of 13.3°. The chord Reynolds number is $2.1 \cdot 10^6$ and the flow is subsonic with a freestream Mach number of 0.15. These are high-lift conditions at take-off and landing. The flow around the Aerospatiale A-airfoil has been the subject of

extensive study. Different CFD codes (steady and unsteady RANS, compressible and incompressible methods) were validated in the EUROVAL project [2] and in the ECARP project [3] on this particular single-element airfoil. It was found that few RANS models are capable of handling this flow problem, mainly because of the lack of curvature effects in the eddy-viscosity models. The second-moment closures (which do take into account curvature effects) produced the best results, see also Refs. [4, 5, 6]. Much because of the rate at which computer power is increasing, LES is becoming an interesting approach applicable for more complex flows.

This is a challenging case for LES owing to the high Reynolds number and because of the different flow regimes around the airfoil, which are sketched in Fig. 3. At the leading edge there is a very thin laminar boundary layer. On the pressure side, this boundary layer is tripped at 30% of the chord and there is a transition to a very thin turbulent boundary layer. On the suction side, there is a peak in the pressure near the leading edge. The favorable pressure gradient accelerates the flow around the leading edge. In this case the flow separates, a separation bubble is formed and, when the flow reattaches at about 12% of the chord, the boundary layer becomes turbulent. The boundary layer grows under the influence of an adverse pressure gradient and, at about 82.5% of the chord, the flow separates. In the wake, downstream of the trailing edge, the low-speed flow from the separation region on the suction side forms a mixed shear layer with the flow from the very thin boundary layer on the pressure side.

Even at the from an aeronautical point of view low Reynolds number, a wall-resolved LES is too expensive. The use of approximate boundary conditions in the near-wall region is necessary and a good method of prescribing and controlling the transition is needed. Still, the requirements on the mesh are demanding and result in meshes with a large number of nodes. For this reason, an efficient numerical method with an effective parallelisation is needed.

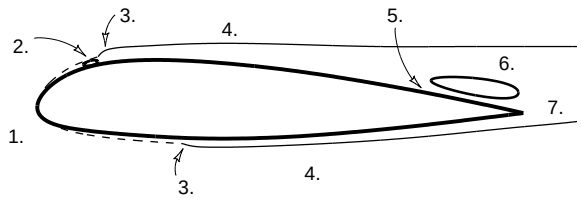

Figure 3: Schematic sketch of the flow regimes around the Aerospatiale A-profile: 1. laminar boundary layer, 2. laminar separation bubble, 3. transition region, 4. turbulent boundary layer, 5. separation point, 6. separation region, 7. wake region.

Results from four computations on two meshes are presented, with focus on the last three, where upwinding is used in part of the domain to prescribe the transition and suppress unphysical oscillations. The outline of this paper is: the following two sections summarise the numerical method and boundary conditions. The upwinding/central difference scheme is presented in section 4.4 and then the two meshes and an approximate boundary condition are described in section 4.5 and 4.6, respectively. The convergence criteria are discussed and speed-up results are presented in section 4.7. In section 4.8 the results are presented and in the last section conclusions are drawn.

4.2 Numerical Method

The code used is an incompressible finite volume Navier-Stokes solver called CALC-BFC [16]. The solver is based on structured grids and the use of curvi-linear boundary fitted coordinates. The grid arrangement is collocated and the Rhie and Chow interpolation method [17] is used. The code is parallelised for 3D flows [18] using block decomposition and the message passing systems PVM and MPI. For the advancement in time, the Crank-Nicolson scheme is used and the momentum equations are discretised in space using 2nd order difference schemes (the central difference scheme (CDS) and the van Leer scheme). The PISO algorithm [22] is used for the pressure-velocity coupling. As a subgrid scale model, the Smagorinsky model is used with the Smagorinsky constant equal to 0.1.

4.3 Boundary Conditions

In the computations on the *UMIST mesh* (see Fig. 6), no-slip condition is applied at the airfoil wall. In the computations on the *Chalmers mesh* (see Fig. 8), the no-slip condition is compared to an approximate wall boundary condition, based on the instantaneous log-law. The inlet is specified all over the curved areas of the C-meshes. The velocities are set to $\overline{u} = \cos\alpha U_\infty$ and $\overline{v} = \sin\alpha U_\infty$, where U_∞ is the freestream velocity. At the outlet, a convective boundary condition is applied: $\frac{\partial\phi}{\partial t} + U_\infty \frac{\partial\phi}{\partial x} = 0$. A Neumann boundary condition is used for the pressure at all boundaries ($\frac{\partial\overline{p}}{\partial n} = 0$) and periodic boundary conditions are used in the spanwise direction.

4.4 Discretisation Schemes of the Convective Terms

When the momentum equations are discretised in space using the central difference scheme (CDS), considerable unphysical oscillations are present all over the computational domain (see Fig. 4). The CDS is often

used in LES because of its non-dissipative and energy-conserving properties. However, the scheme is also known to produce these odd-even oscillations (grid-to-grid oscillations or wiggles) when the resolution is poor.

To remove the unphysical oscillations in front of the airfoil and upstream of the transition region, a bounded second-order upwind discretisation scheme (the van Leer scheme) is used in this region. The schemes are blended in the transition region, so that the convective flux can be expressed as:

$$\dot{m}u^m_{UDS} + \dot{m}\left[\alpha u^{m-1}_{CDS} - \alpha u^{m-1}_{UDS} + (1-\alpha)u^{m-1}_{UDScorr}\right] , \tag{34}$$

where CDS stands for the central difference scheme, UDS for the 1st-order upwind scheme and $UDScorr$ for the 2nd-order correction to the lower order upwind scheme ($m-1$ is the previous iteration). Here α is a blending function ($0 \leq \alpha \leq 1$) and, at the extremes, we have:

$\alpha = 0$: the van Leer scheme
$\alpha = 1$: the central difference scheme with deferred correction

The blending function used in the computation on the UMIST mesh blends the two schemes from 1 to 8 % of the chord on the suction side and from 4 to 19 % on the pressure side.

Upwinding removes unphysical oscillations, not only in the part of the domain where upwinding is used but also downstream of the area where the mixing between the two schemes is applied. This can be seen in Fig. 5, where the resolved stresses in the wall-normal direction are

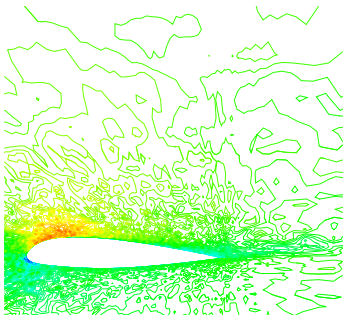

Figure 4: Instantaneous $\overline{u}$-velocity when central differencing is used on the UMIST mesh (Comp. # 1).

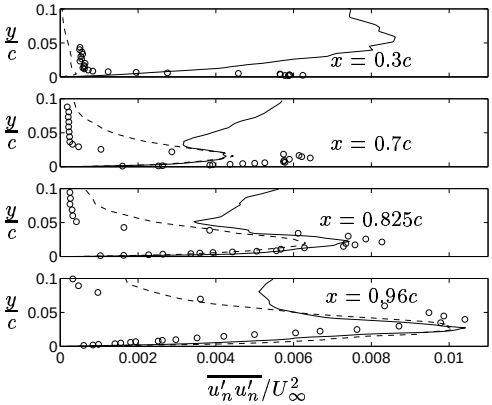

Figure 5: Spanwise and time averaged resolved $\overline{u'_n u'_n}$-velocity fluctuations. Solid: Comp. # 1 (CDS); dashed: Comp. # 2 (upwinding); circles: exp. (F2).

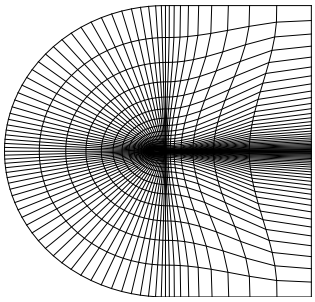

Figure 6: The UMIST mesh: $321 \times 65 \times 33$ nodes (every 4th node in the i-direction and every 2nd node in the j-direction are plotted).

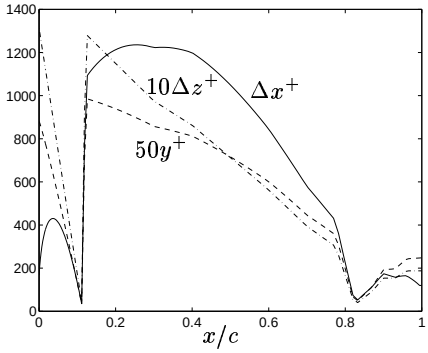

Figure 7: The size of the cell and the distance to the nearest node in dimensionless wall units along the suction side of the airfoil wall on the UMIST mesh ($L_z = 0.03c$).

shown. Note that not all unphysical oscillations are absent in the CDS-region (mainly because of the coarse resolution in the streamwise direction). These result in high values of the resolved stresses, in the outer parts of the boundary layer (see Fig. 5).

4.5 Meshes

Although the unphysical oscillations are suppressed and dampened upstream respectively downstream of the transition region, the present grid, the UMIST mesh (see Fig. 6), is far too coarse to be able to do a useful LES. The mesh consists of $321 \times 65 \times 33$ grid-nodes; the resolution on the suction side of the airfoil is shown in Fig. 7. In order to be able to do a useful LES when wall functions are used, the size of the cells in the streamwise direction near the wall should be less than 600 wall units [10]. Judging from this limit, the resolution is very poor. Δx^+ exceeds 1200 and the maximum is in the transition region. Besides, the no-slip condition is used.

A new mesh was constructed (see Fig. 8) that consists of $720 \times 65 \times 33$ nodes, more than twice as many nodes in the i-direction (the wrap-around-direction in the C-mesh). Fig. 9 shows the wall resolution on the suction side of the airfoil on the new mesh. Here, Δx^+ does not exceed 600. Δx is increased linearly from the leading edge to the trailing edge on the suction side and the stretching is very low (which is crucial for the energy conservation, see e.g. [24]) Overall, the stretching in this direction is less than 5.9% (the maximum is in the wake near the trailing edge). Besides the resolution in the i-direction, this is one of the

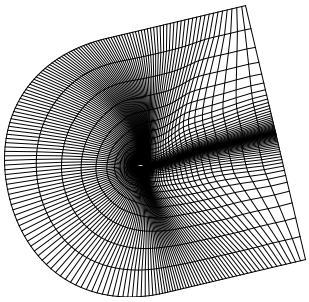

Figure 8: The Chalmers mesh: $720 \times 65 \times 33$ nodes (every 4th node in the i-direction and every 2nd node in the j-direction are plotted).

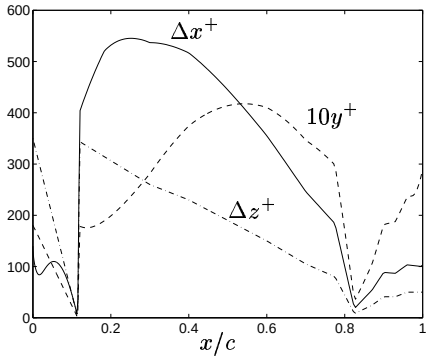

Figure 9: The size of the cell and the distance to the nearest node in dimensionless wall units along the suction side of the airfoil wall on the Chalmers mesh ($L_z = 0.08c$).

main differences as compared with the former mesh, in which the maximum stretching is 29.2% (just downstream of the trailing edge). Other differences are that the new mesh is refined along the wake and that the resolution in the wall-normal direction near the trailing edge and in the wake is much coarser on the new mesh, which can be a problem in the wake where the mixed shear layer should be sufficiently resolved.

4.5.1 The resolution and extension in the spanwise direction

The extent in the spanwise direction for the airfoil case was initially chosen as $L_z = 0.03c$. Near the trailing edge, however, the boundary layer thickness, δ_{99}, from the experiments, is about 9 % of the chord, three times larger than L_z. When periodic boundary conditions are used, these conditions imply that the extent in the spanwise direction should be wider than the largest structures in that direction. The largest scales in a boundary layer are in the order δ_{99} and these scales are probably also apparent in the spanwise direction; thus the ratio δ_{99}/L_z should at least be less than one. L_z was set to $0.08c$ on the Chalmers mesh. Thirty-two cells are used in the spanwise direction for both meshes, resulting in almost three times coarser resolution compared to the UMIST mesh and Δz^+_{max} is approximately 350 on the Chalmers mesh (in Figs. 7 and 9 the wall units ($\frac{u_\tau}{\nu}$) are computed from the skin friction coefficient from the experimental data, the y^+ and Δz^+ from the predicted friction velocity are shown in Figs. 18 and 20).

4.6 Approximate Wall Boundary Conditions

In a wall-resolved LES, the distance from the wall to the first node should be at least less than two wall units ($\frac{u_\tau}{\nu}$). Although the velocity profile in the viscous sublayer ($y^+ < 5 - 8$) is linear in the mean, instantaneously this need not be the case and y^+ must be less than two in order to resolve the velocity gradient close to the wall. In addition however, in a wall-resolved LES, the structures close to the wall, especially the important energy-producing structures, need to be sufficiently resolved. There are streamwise counter-rotating vortices in the viscous sublayer, the *streaks*. These structures have an approximate spanwise periodicy of 100 wall units and a length of 1000 wall units. It is important to capture these near-wall streaks as they interact with the buffer region and are responsible for a major part of the energy production in this region through the *bursting* process [13]. Other mechanisms in the buffer region are *sweeps* (when high-speed fluid from the logarithmic region enters the buffer region) and *ejections* (when low-speed fluid from the buffer region enters the logarithmic region). All these coherent structures can be captured in a wall-resolved LES if the sizes of the cells closest to the wall are within the range of $50 < \Delta x^+ < 150$, $\Delta y^+ < 4$ and $15 < \Delta z^+ < 40$ [10].

A wall-resolved LES of the near-wall streaks in the turbulent boundary layer on the airfoil is not feasible owing to the required computer power. At this high Reynolds number ($Re_c = 2.1 \cdot 10^6$), the near-wall problem of LES is evident. The use of approximate wall boundary conditions are necessary. Grids with a lot coarser resolution in the spanwise and streamwise directions are then used and the first node from the wall is placed in (the buffer region or) the logarithmic region. With such a grid, many of the coherent structures will not be sufficiently resolved and the sublayer streaks are not resolved at all.

Numerically, when the near-wall resolution is insufficient, the correct value of the wall shear stress ($\tau_{wall} = \nu \left(\partial \overline{u}/\partial y\right)_{wall}$) needs to be determined. The wall shear stress is usually assumed to be correlated to the velocity in the log region through the use of a near-wall law, e.g. the power law or the log law. In the present work the instantaneous log law is used in the log region ($y^+ \geq 30$):

$$\bar{u}^+ = \frac{\ln y^+}{\kappa} + B \,, \tag{35}$$

where $\kappa = 0.4$, $B = 5.2$.

The wall-normal cell size (Δy) at the leading and trailing edge must be very small in order to sufficiently resolve the very thin laminar boundary layer and the mixed shear layer. When generating meshes, this will result in the cells having small Δy in the wall-bounded turbulent boundary layers as well. For that reason, the y^+ may often be located in the

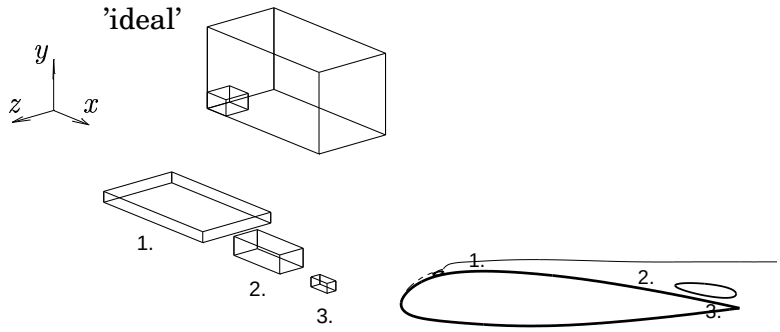

Figure 10: The size of the cells in dimensionless wall units on the Chalmers mesh compared with the 'ideal' size when wall functions are used (the smaller box $= [100, 60, 100] < [\Delta x^+, \Delta y^+, \Delta z^+] < [600, 300, 300] =$ the larger box): 1. just after the transition, 2. before the separation, 3. in the separation region ($L_z = 0.08$, 32 cells in the spanwise direction).

buffer region ($5 \leq y^+ \leq 30$) in which the following wall law is used:

$$\bar{u}^+ = \frac{\ln y^+}{C} + D \ . \tag{36}$$

Eq. 36 is a matching between the log law (Eq. 35) and the linear law in the viscous sublayer ($y^+ \leq 5$):

$$\bar{u}^+ = y^+ \ . \tag{37}$$

The constants in Eq. 36 becomes $C = \ln 6/(\frac{1}{\kappa}\ln 30 + B - 5)$ and $D = 5 - C\ln 5$.

These wall functions (Eqs. 35-37) are compared to the no-slip condition in the computations on the Chalmers mesh. The relation between the cells compared to the 'ideal' size is visualized in Fig. 10 at three different streamwise locations, just after the transition, before the separation and in the separation region. The 'ideal' size refers to a resolution of $[100, 60, 100] < [\Delta x^+, \Delta y^+, \Delta z^+] < [600, 300, 300]$ [10]. In addition, the ratio between Δz^+ and Δy^+ should preferably be in the order of one [25]. This is not the case just after the transition as can be seen in Fig. 10, where $\left(\frac{\Delta z^+}{\Delta y^+}\right)_{max} \approx 10$.

The approximate wall boundary condition is implemented in the code by adding a viscosity, $\nu_{B.C.}$, to the laminar viscosity on the wall. The friction velocity, u_τ (and τ_{wall}), is determined from Eqs.35-37. From the relation

$$\frac{\tau_{wall}}{\rho} = u_\tau^2 = \nu \frac{\partial \bar{u}}{\partial y}\bigg|_{wall} = (\nu + \nu_{B.C.})\frac{\bar{u}_P}{y_P} \ , \tag{38}$$

the viscosity on the wall could be expressed as

$$\nu + \nu_{B.C.} = \frac{u_\tau y_P}{\bar{u}_P^+} \,. \tag{39}$$

Note that the numerical boundary condition for $\overline{u}$, $\overline{v}$ and $\overline{w}$ at the wall is no-slip according to Eq. 38. The product of the artificial viscosity at the wall, $\nu+\nu_{B.C.}$, and the linear velocity assumption between the near-wall node and the wall (see Eq. 38) give the wall shear stress τ_{wall} according to the wall functions.

4.7 Efficiency of the Parallelisation

For the present flow, the required number of nodes in order to do a LES is in the order of millions. This is true, even though the transition is prescribed and the effects of the very near-wall structures are modeled by approximate boundary conditions. It is also estimated that about $10-20$ time units (1 time unit $= c/U_\infty$, where c is the airfoil chord and U_∞ is the freestream velocity) of simulation are required to be able to gather reliable statistics; with a time step of $3 \cdot 10^{-4} c/U_\infty$ (the present time step), the number of time steps would be at least 33000. The need for an efficient numerical method and effective parallelisation is obvious. The present code is parallelised for 3D flows [18] using block decomposition and PVM and MPI as message passing systems. The code has been ported to a SUN Enterprise 10000 at Chalmers and the IBM SP at the Center for Parallel Computing at KTH.

4.7.1 Convergence criteria

For the velocities, the convergence criteria is that the L^1-norm of the residuals of the discretised momentum equations scaled with $\rho U_\infty A_{inlet} U_\infty$ should be less than the desired convergence level, η, where A_{inlet} is the projected area of the inlet. Here, the criteria is checked immediately after the solver (but of course without under-relaxation), i.e. the residuals are calculated with the 'old' coefficients and before the correction in the PISO algorithm. For the continuity equation, the criterion is that the L^1-norm of discretised finite-volume continuity error scaled with the inlet mass flow should be less than η.

In the computations on the UMIST mesh, the convergence level is set to $1 \cdot 10^{-3}$ and with a time step of $3 \cdot 10^{-4} c/U_\infty$, there are three global iterations per time step for Comp. # 1 which decreases to two iterations for Comp. # 2 (the one with upwinding scheme, see Table 2). In these two computations, the convergence criteria for the continuity equation is well fulfilled (it is fulfilled immediately at each time step). The scaled L^1-norm is approximately $1 \cdot 10^{-4}$. It is notable that the

Mesh	Computer & message passing system	Number of processors 8	16	32
UMIST	SUN, PVM, socket based	$48s$	$38s$	$36s$
	SUN, PVM, shared memory based	$24s$	$(12s)$	$(6s)$
	SUN, MPI	$24s$	-	-
	IBM SP, PVM	$12s$	-	-
	IBM SP, MPI	-	$5.4s$	$2.8s$
Chalmers	IBM SP, MPI	-	-	$6.0s$

Table 1: Elapsed time per timestep on the UMIST and Chalmers meshes (722568 and 1617924 computational nodes, respectively).

convergence within each time step is very slow. The PISO algorithm [22] is used for the pressure-velocity coupling, with two additional corrector steps beside the first SIMPLE step. The algorithm was found to be more efficient than the optimized SIMPLEC algorithm in a previous study on a backward-facing step flow [26]. In the present airfoil case, it is the convergence of the pressure-correction equation that sets the limit on the convergence rate, at least for the computations on the finer mesh (the Chalmers mesh). Here, the scaled L^1-norm is approximately $1 \cdot 10^{-3}$ and sometimes exceeds the convergence level, η. Because of the very slow convergence within each time step, the approach of simply limiting the number of global iterations per time step is applied. For the computations on the Chalmers mesh, the number of iterations is set to two, corresponding to an η of approximately $1 \cdot 10^{-3}$.

4.7.2 Speed-up results

The elapsed time per time step is shown in Table 1 with the convergence criteria fulfilled after two global iterations ($\eta \approx 1 \cdot 10^{-3}$). The computational domain is decomposed into eight, 16 and 32 subdomains. No significant decrease in the convergence rate is observed when 16 and 32 subdomains are used. Two different versions of the message passing PVM are available on the SUN computer: a shared memory based PVM and a socket based PVM. When eight processors are used for the present case, the shared memory based PVM is twice as fast as the socket based PVM. The simulation of one time unit requires about 180 CPU hours and the solution is advanced in time by about one time unit per day.

The IBM SP computer is faster. The simulation of one time unit requires about 83 CPU hours and with MPI and 32 processors the solution is advanced 9 time units per day. On this computer, an approximately linear speed-up is obtained between the eight and 32 processor cases. On the finer mesh, the elapsed time per time step is $6s$ and the simulation of one time unit requires about 180 CPU hours. The solution is

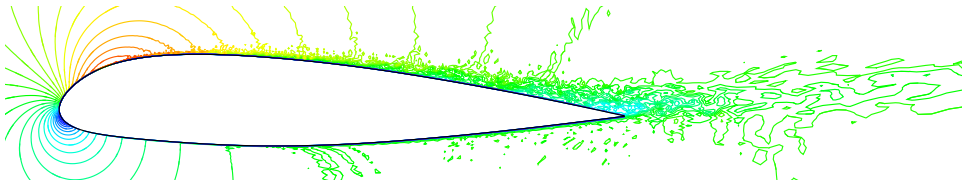

Figure 11: Instantaneous $\bar{u}$-velocity on the Chalmers mesh when wall functions are used (Comp. # 4).

Computation	**# 1**	**# 2**	**# 3**	**# 4**
Mesh	UMIST $321 \times 65 \times 33$		Chalmers $720 \times 65 \times 33$	
Spanwise ext.	$L_z = 0.03c$		$L_z = 0.08c$	
Convective scheme	CDS	van Leer ($x/c < 0.01$) + CDS ($x/c > 0.09$)	van Leer ($x/c < 0.02$) + CDS ($x/c > 0.12$)	
SGS model	Smagorinsky		no model ($x/c < 0.12$) + Smagorinsky ($x/c > 0.23$)	
Wall b. c.	⟵ no-slip ⟶			Eqs. 35-37

Table 2: Computational parameters that differ for the four computations. The Smagorinsky constant is set to 0.1.

advanced more than four time units per day, which is quite acceptable for industrial use.

4.8 Results

Four computations are presented in this paper. The set-up differences are summarised in Table 2. The averaging times are at least six time units, which is checked to be reasonably sufficient, even for second-order statistics, when the boundary layer remains attached. The initial conditions are 2D $k-\varepsilon$ solutions for Comp. # 1 and # 3 and the previous LES for Comp. # 2 and # 4. The time step is $3 \cdot 10^{-4} c/U_\infty$ for all computations, giving a maximum CFL number of 1.3 for Comp. # 1. When upwinding is used on the UMIST mesh it decreases a great deal ($CFL_{max} \approx 0.6$). For the computations on the finer mesh, the maximum CFL number is approximately 1.

In the computations on the Chalmers mesh, the extent of the mixing region between the two schemes were moved slightly downstream in order to more accurately prescribe the transition at the location given in the experiments (at 12% of the airfoil chord). The CDS is fully active

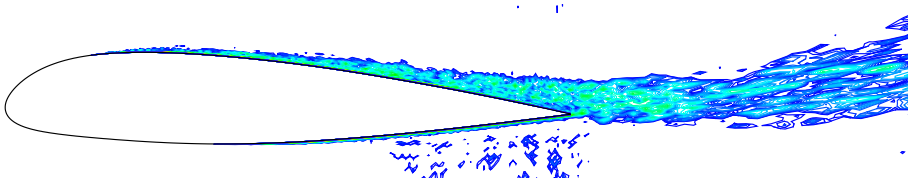

Figure 12: Instantaneous Smagorinsky eddy viscosity on the Chalmers mesh when wall functions are used (Comp. # 4). The contour levels are logarithmic.

just downstream of that point and is gradually mixed with the van Leer scheme, which is fully active upstream of location $x = 0.02c$. In the Smagorinsky model, the eddy viscosity is not zero in the laminar region (the strain is not zero). To prescribe the transition in a more accurate way, the Smagorinsky eddy viscosity is set to zero upstream of the transition point and is gradually mixed with the eddy viscosity downstream of that point. At 23% of the airfoil chord, the Smagorinsky model is fully active. A similar approach is applied around the transition point on the pressure side of the airfoil.

The transition and growth of the turbulent boundary layer is clearly visualized in the computations on the finer mesh, when looking at instantaneous contourplots of the resolved velocity and the Smagorinsky eddy viscosity (see Figs. 11 and 12). The very thin turbulent boundary layer on the pressure side is also visible in the figures, as well as some unphysical oscillations outside of the thin layer, owing to a coarser resolution in the streamwise direction on this side. A contour plot of the instantaneous resolved pressure is shown in Fig. 13.

Although the resolution is increased in the streamwise direction and approximate wall boundary conditions are applied, the pressure peak at the leading edge is underpredicted and we fail to predict the plateau, the decrease in the adverse pressure gradient, that should be present in the separation region (see C_p in Fig. 14). Consequently none of the present computations predict the separation near the trailing edge (a small separation bubble is occasionally instantaneously formed) and the

Figure 13: Instantaneous resolved pressure on the Chalmers mesh when wall functions are used (Comp. # 4).

skin friction coefficient remains positive (see Fig. 14).

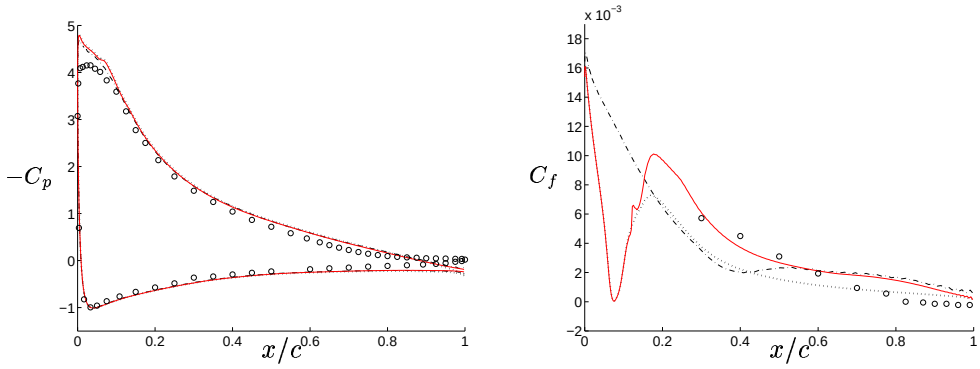

Figure 14: The pressure coefficient (left figure) and the skin friction coefficient (right figure). Red solid: approximate wall boundary condition, Eqs. 35-37 (Comp. # 4); dotted: no-slip wall boundary condition (Comp. # 3); dash-dotted: Comp. # 2; circles: exp. (F2).

4.8.1 Effect of the approximate wall boundary condition

Comparing Comp. # 4 and # 3, the use of the approximate wall boundary condition (Eqs. 35-37) has a significant effect on the results (see e.g. Fig. 22). Looking at the artificial viscosity at the wall (Fig. 15), this is not great compared with the values at the near-wall node (Fig.16), but it works to decrease the eddy viscosity at the near-wall node, which is located in the lower parts of the logarithmic region (see Fig. 18). The eddy viscosity is increased further away from the wall as compared with when the no-slip condition is used (see Fig. 17).

4.8.2 Transition

When α is larger than approximately 0.6 in the mixed scheme (see Eq. 34 and Table 2), the non-dissipative effects of the CDS give rise to numerical oscillations and the boundary layer is tripped numerically. The resolved stresses at the near-wall node (shown in Fig. 19) are very high, especially in the x-direction. Unfortunately, no experimental data are available in the transition region, but for Comp. # 3, the $\overline{u'u'}$-peak is almost five times larger than the maximum stresses from the experiments near the trailing edge. The Smagorinsky eddy viscosity at the same near-wall nodes (Fig 16), in the beginning of the mixed region (e.g. at $x = 0.15c$), is very low. The CDS is fully active already at 12% of the chord, suggesting that the maximum peaks in the stresses (at about 13% of the chord) are unphysical and due to the central difference scheme alone. The unresolved stresses should most likely account for a

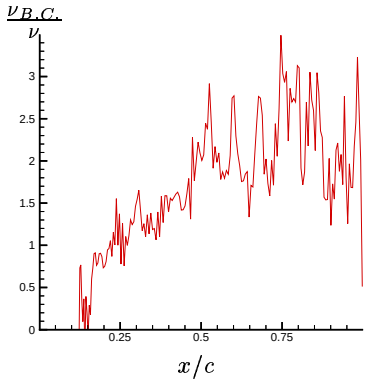

Figure 15: Instantaneous viscosity $\nu_{B.C.}$ on the wall, see Eq. 39 (Comp. # 4).

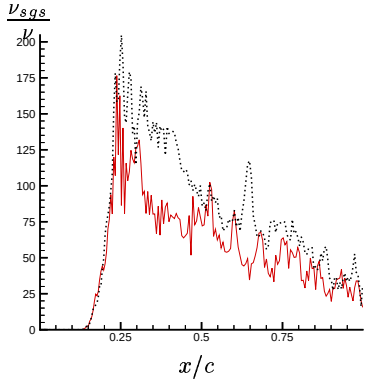

Figure 16: Instantaneous Smagorinsky eddy viscosity at the near-wall node. Red solid: approximate wall boundary condition, Eqs. 35-37 (Comp. # 4); dotted: no-slip wall boundary condition (Comp. # 3).

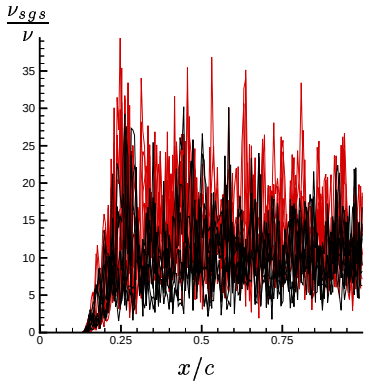

Figure 17: Instantaneous Smagorinsky eddy viscosity at nodes 2 to 9 from the wall. Red: approximate wall boundary condition, Eqs. 35-37 (Comp. # 4); black: no-slip wall boundary condition (Comp. # 3).

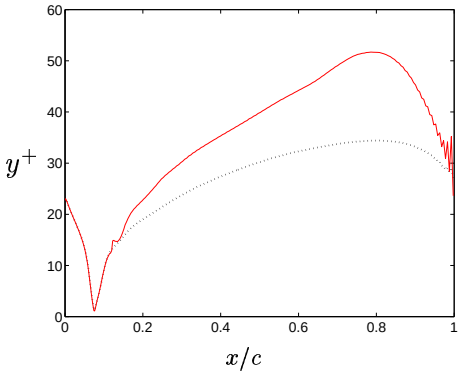

Figure 18: Spanwise and time averaged wall distance (in dimensionless wall units $y^+ = yu_\tau/\nu$) at the near-wall node based on the predicted friction velocity. Red solid: approximate wall boundary condition, Eqs. 35-37 (Comp. # 4); dotted: no-slip wall boundary condition (Comp. # 3).

significant part of the stresses (using these coarse grids in the transition region) and the transition could be prescribed more accurately by letting the Smagorinsky model damp the resolved stresses in the tran-

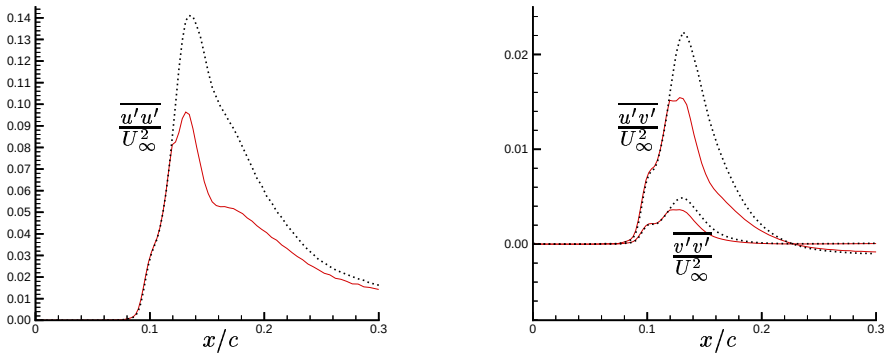

Figure 19: Spanwise and time averaged resolved velocity fluctuations at the near-wall node in the transition region. Red solid: approximate wall boundary condition, Eqs. 35-37 (Comp. # 4); dotted: no-slip wall boundary condition (Comp. # 3).

sition region.

The approximate wall boundary condition has an dampening effect on the resolved stresses, in the transition region and a bit downstream (from 12 to approximately 30 percent of the chord, see Fig. 19). Further downstream (see Fig. 22), the wall functions increase the magnitude of the stresses and they are closer to the experimental results.

4.8.3 Resolution in the streamwise and spanwise directions

The effect of the increased streamwise resolution is for instance seen in the outer parts of the boundary layer (see Fig. 22). Not only the resolved stresses, but also the eddy viscosity, goes down to zero in the outer parts. This is seen in the sharp boundary layer edges in the velocity profiles. The major difference between Comp. # 2 and the computations on the Chalmers mesh is seen in the skin friction coefficient, where Comp. # 2 completely fails to capture the laminar separation bubble, contrary to Comp. # 3 and # 4, where there is a clear indication of the laminar separation bubble at about 7% of the chord (see Fig. 14). Also note the little plateau in the pressure coefficient, indicating separation.

Although incorrectly predicted, the effect of the small spanwise extent need not be that significant, in these attached boundary layer computations. The maximum boundary layer thickness near the trailing edge is about $4-5\%$ of the chord and $L_z = 0.03c$ may be enough to resolve the largest structures in that direction (see Sec. 4.5.1).

It is notable that we get worst results for Comp. # 3 and very similar results for computation # 2 and # 4 around the rear part of the airfoil

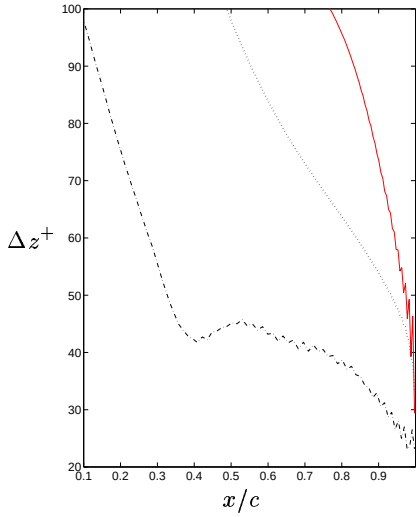

Figure 20: Spanwise and time averaged resolution in the spanwise direction based on the predicted friction velocity (in dimensionless wall units $\Delta z^+ = \Delta z u_\tau / \nu$). Red solid: Comp. # 4; dotted: Comp. # 3; dash-dotted: Comp. # 2

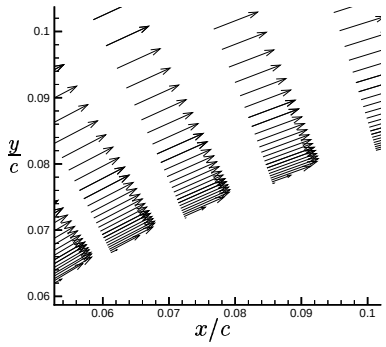

Figure 21: Vector plot of the laminar boundary layer at the leading edge showing incipient separation (every 7th vector in the streamwise direction is shown).

($x/c > 0.5$). This is true for the velocity profiles as well as the magnitude of the shear stresses (see Fig. 22). This might be an effect of the spanwise resolution. As seen in Fig. 20, the *computed* spanwise resolution (based on the predicted friction velocity) for Comp. # 2 is less than 45 wall units at the rear 65% of the profile. It is likely that the near-wall streaks is starting to be resolved, thanks to the spanwise resolution. This is also noted as an increase in the skin friction coefficient (see Fig 14). This increase in C_f is not seen for Comp. # 3 (where the computed Δz^+ never gets fine enough to resolve the near wall streaks (see Fig. 20)) and not for Comp. # 4 either, but the approximate wall boundary condition seems to take these effects into account, right from where the transition starts. The spanwise resolution seems to be very important, in that Comp. # 3 with a finer resolution in the streamwise direction, produces worse results than Comp. # 2. It is encouraging that the wall functions seem to have their intended effect and handle the coarse spanwise resolution.

4.8.4 Lift and drag coefficients

Table 3 shows the lift and drag coefficients for the different computations. The lift coefficients from the computations are overpredicted.

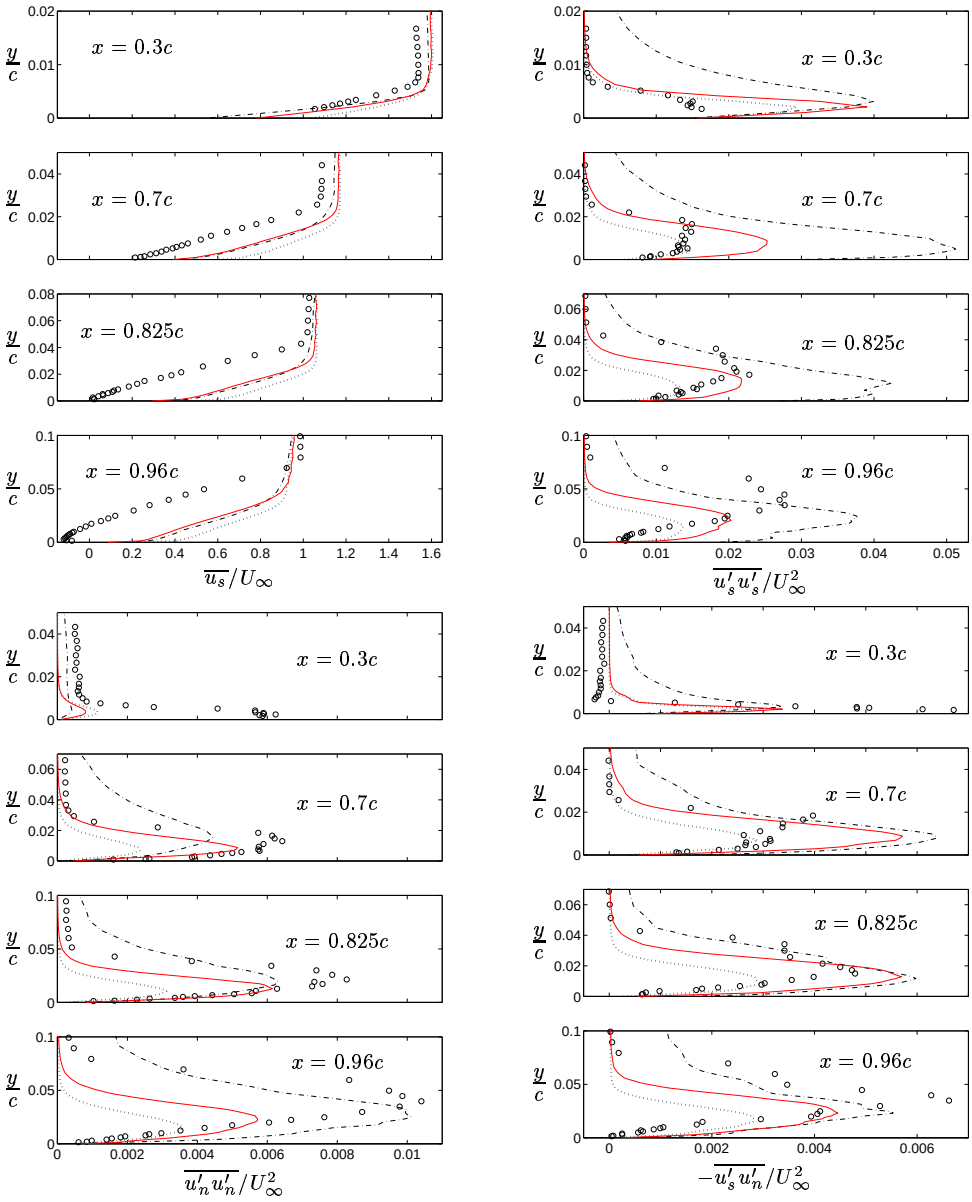

Figure 22: Spanwise and time averaged first- and second-order statistics. Red solid: approximate wall boundary condition, Eqs. 35-37 (Comp. # 4); dotted: no-slip wall boundary condition (Comp. # 3); dash-dotted: upwinding scheme on the UMIST mesh (Comp. # 2); circles: exp. (F2). Subscripts s and n denote the directions parallel and normal to the airfoil wall, respectively.

They increase somewhat when upwinding is used. The drag coefficients decrease significantly when upwinding is used and even more for Comp. # 3 and # 4. Comparing Comp. # 3 and # 4, there is a tendency toward the experimental results when the approximate boundary condition is used.

	Exp. F1	# 1	# 2	# 3	# 4
C_L	1.56	1.68	1.72	1.75	1.72
C_D	0.0204	0.0374	0.0280	0.0167	0.0170

Table 3: Spanwise and time averaged lift and drag coefficients for the four computations and the experiment in the F1 wind-tunnel.

Figs. 23-25 show the time history of the lift and drag coefficients. It is interesting to note that the drag coefficient varies between approximately 0.013 and more than twice that (0.0275). Fig. 26 shows the frequency spectrum of the lift coefficient. Although the magnitude of the oscillations vary a lot, there is a distinct peak in the frequency spectrum at a Strouhal number of 8.6.

4.9 Conclusions and Future Work

Although none of the present computations predict separation, it is encouraging that the wall functions seem to take into account the low resolution in the spanwise direction (in these attached boundary layer simulations) and hope is that this is true in the other directions as well.

The transition process and the behaviour of the SGS-model and CDS in that region also need further examination to prescribe the transition in a more natural way.

However, one of the major problems seem to be in the laminar region and the resolution of the laminar boundary layer. It is in this

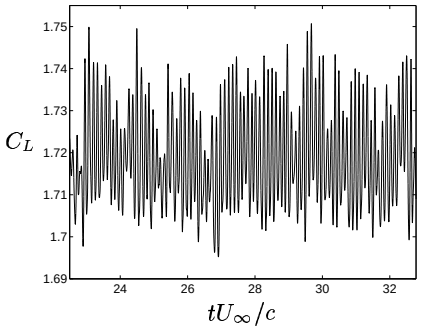

Figure 23: Time history of the lift coefficient for Comp. # 4.

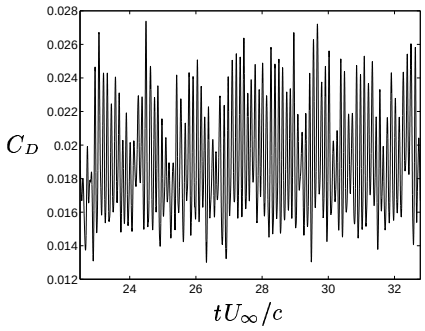

Figure 24: Time history of the drag coefficient for Comp. # 4.

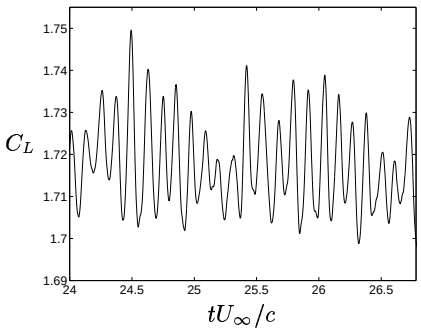

Figure 25: Time history of the lift coefficient for Comp. # 4.

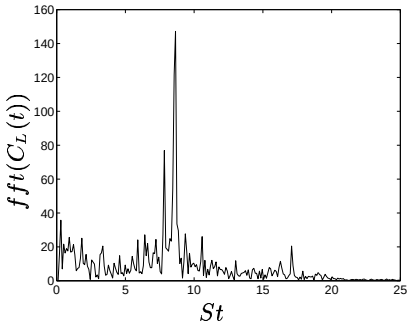

Figure 26: Frequency spectrum of the C_L signal for Comp. # 4.

region, around the leading edge, where the favorable pressure gradient accelerates the flow. This accelerated flow, certainly affects the region downstream and has an impact on the separation near the trailing edge. It is evident from the results (C_f, the underpredicted pressure at the leading edge and the overpredicted boundary layer edge velocity (at e.g. $x = 0.3c$)) that the simulations have failed at the leading edge. In the computations, at the location where the boundary layer is as thickest, there are about 4-5 nodes in the wall-normal direction (see Fig. 21). And at the very leading edge ($x/c < 0.01$) there is only one node in the boundary layer. The resolution must probably be finer in this direction, making the prediction of the flow in this region more accurate. Alternatively, some approach (e.g. wall functions) must be applied in this region.

Furthermore, the separation region near the trailing edge is fairly thin and the use of a y^+ requirement for wall functions does not make any sense here. The separation region needs to be sufficiently resolved, not in a DNS-sense, but in the sense that a sufficient number of cells are used close to the wall to resolve the maximum backflow velocity [27]. In the Chalmers mesh, this region is captured with just 1-2 cells (in the wall-normal direction) downstream of the separation point, in the streamwise center of the separation bubble. This is inadequate and a modified mesh has been generated which will be used in the near future.

Acknowledgements

The LESFOIL project (Project No. BRPR-CT97-0565) is financed by the Brite-Euram programme.

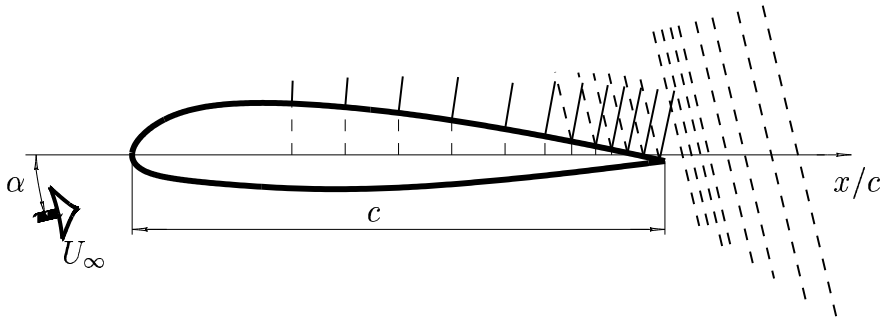

Figure 27: The Aerospatiale A-airfoil and the experimental geometry. solid: data normal to the airfoil surface, dashed: data normal to the freestream velocity, U_∞.

5 Complementary Information on the Airfoil Calculations in Chapter 4

This chapter presents some additional results from the airfoil computations described in Chapter 4.

5.1 Measurements

The flow around the Aerospatiale A-airfoil is at an angle of attack, α, equal to 13.3° (see Fig. 27). Based on the far-field velocity U_∞ and the chord of the airfoil, c, the Reynolds number is $2.1 \cdot 10^6$.

Measurements have been carried out in the ONERA F2 windtunnel, not only for the 13.3°-case but also at incidences of 7.2° and 12.3°. The transition on the pressure side was prescribed in the experiments at 30% of the chord. The transition on the suction side was found at 12% of the chord, after the reattachment of a laminar separation bubble.

Experimental data are available in the direction normal to the airfoil surface and normal to the freestream velocity, U_∞, at those locations shown in Fig. 27. At these locations there are velocity profiles (U_s and U_n) as well as normal and shear stress profiles ($\overline{u_s u_s}$, $\overline{u_n u_n}$ and $\overline{u_s u_n}$). In Figs. 28-37 the spanwise and time averaged results for Comp. # 2-4 are compared with the experimental data at the locations shown in Fig. 27.

There are also measurements of the pressure coefficient, C_p, along both the pressure and suction sides of the profile and data on the skin friction coefficient, C_f, the displacement thickness, δ^*, and the momentum thickness, Θ, on the suction side of the airfoil. The lift coefficient, C_L, and the drag coefficient, C_D, have also been measured. C_p and C_f are shown in Fig. 14 in the previous chapter. In Table 3 at p. 32 the computed C_L and C_D are found, here compared with another experiment,

carried out in the ONERA F1 wind tunnel. The lift and drag coefficients are believed to be under- respectively over-estimated in the F2 experiments. More details about the experiments can be found in [28].

Although the simulations clearly fail to predict separation it is interesting to look at the near wall behaviour of the computations. Comparing Comp. # 3 with Comp. # 4, it is seen that the approximate wall boundary condition improves the results.

As concluded in the previous chapter, the transition is unnatural. Looking at the resolved stresses in Figs. 30-32 there is an inaccurate anisotropy in the stresses. The wall-parallel stresses ($\overline{u_s' u_s'}$) are far too high and the wall-normal stresses ($\overline{u_n' u_n'}$) are clearly underpredicted. Note the very high $\overline{u_s' u_s'}$ for Comp. # 2. These unphysical oscillations decreases for Comp. # 3 and 4, where the Chalmers mesh, with a much finer streamwise resolution, is used.

Results from the wake region are shown in Figs. 33-37 and the inaccurate predictions of the velocity profiles in the boundary layers are seen in the wake profiles. It is interesting to note the effect of the approximate wall boundary conditions on the pressure side on the stresses in the wake. The stress levels (resulting from the pressure side flow) are much better predicted for Comp. # 4.

5.2 Complexity of the Flow Case

As seen in Fig. 14, the pressure coefficient is underpredicted (the suction peak is overpredicted) near the leading edge and the computations fail to predict the separation near the trailing edge, the adverse pressure gradient does not decrease sufficiently. Noted should that the sharp suction peak in the pressure coefficient near the leading edge is characteristic of an attached flow. When a separation bubble is formed near the trailing edge, the effective shape of the airfoil is changed and, through the circulation, the suction peak becomes characteristicly smoother (see the experimental data in Fig. 14). Thus, the performance of a model in the downstream part of the boundary layer is directly seen in the C_p-curve around the leading edge. In a simulation where the suction peak is overpredicted, it should be noted that it is not obvious that the method is insufficient in the leading edge region and that it needs improvement in particularly that region. However, this seems to be the case in the present study.

Of course, we do not expect our present model, the Smagorinsky model, to perform 'perfect' (satisfactory) with the simple wall functions used (based on an instantaneous log law throughout the adverse pressure gradient flow) and because of the chosen value of the Smagorinsky constant, C_S, which is not applicable all over the flow field. However, the treatment of the laminar region is believed to have a greater impact

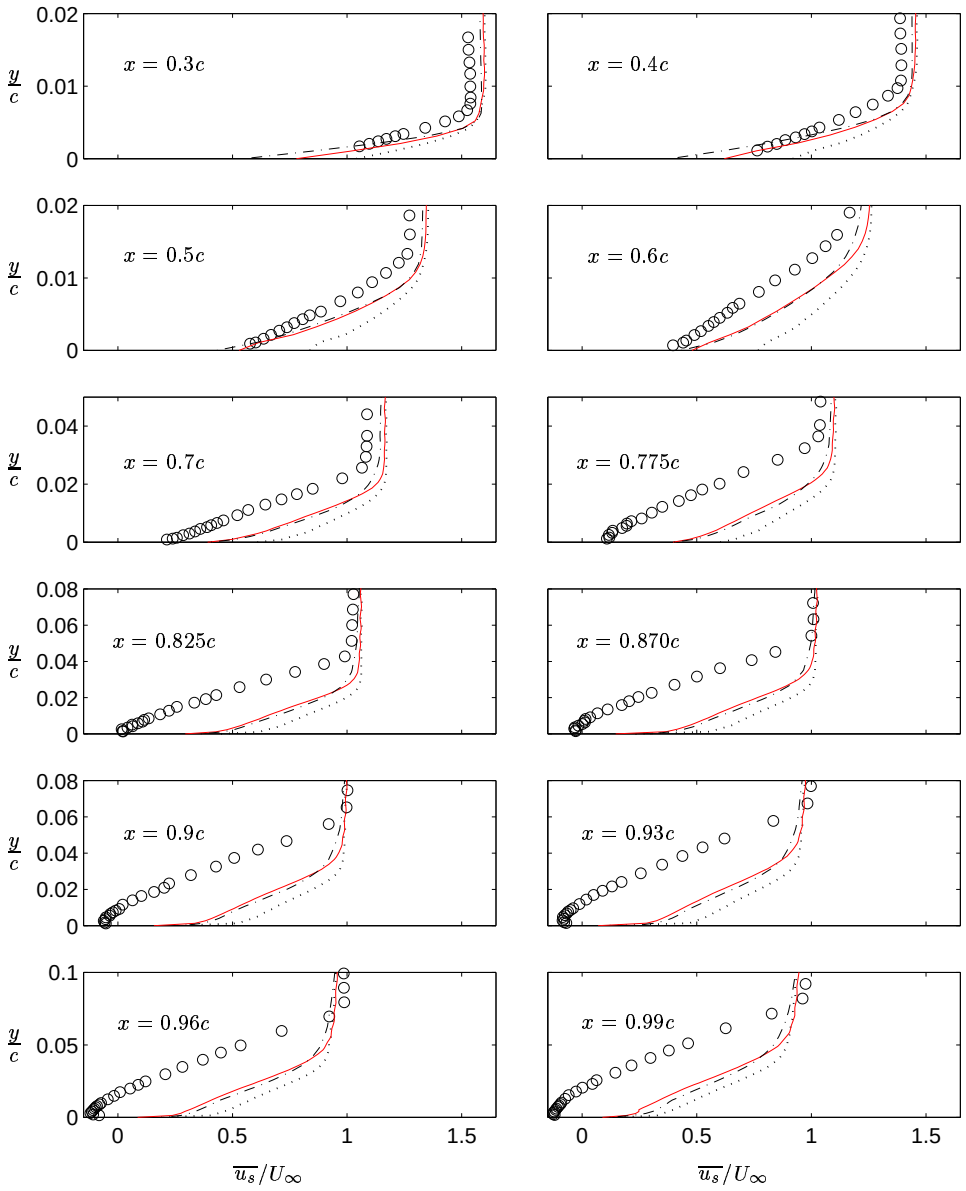

Figure 28: Spanwise and time averaged $\overline{u_s}$-velocity. Red solid: approximate wall boundary condition, Eqs. 35-37 (Comp. # 4); dotted: no-slip wall boundary condition (Comp. # 3); dash-dotted: upwinding scheme on the UMIST mesh (Comp. # 2); circles: exp. (F2). Subscripts s and n denote the directions parallel and normal to the airfoil wall, respectively.

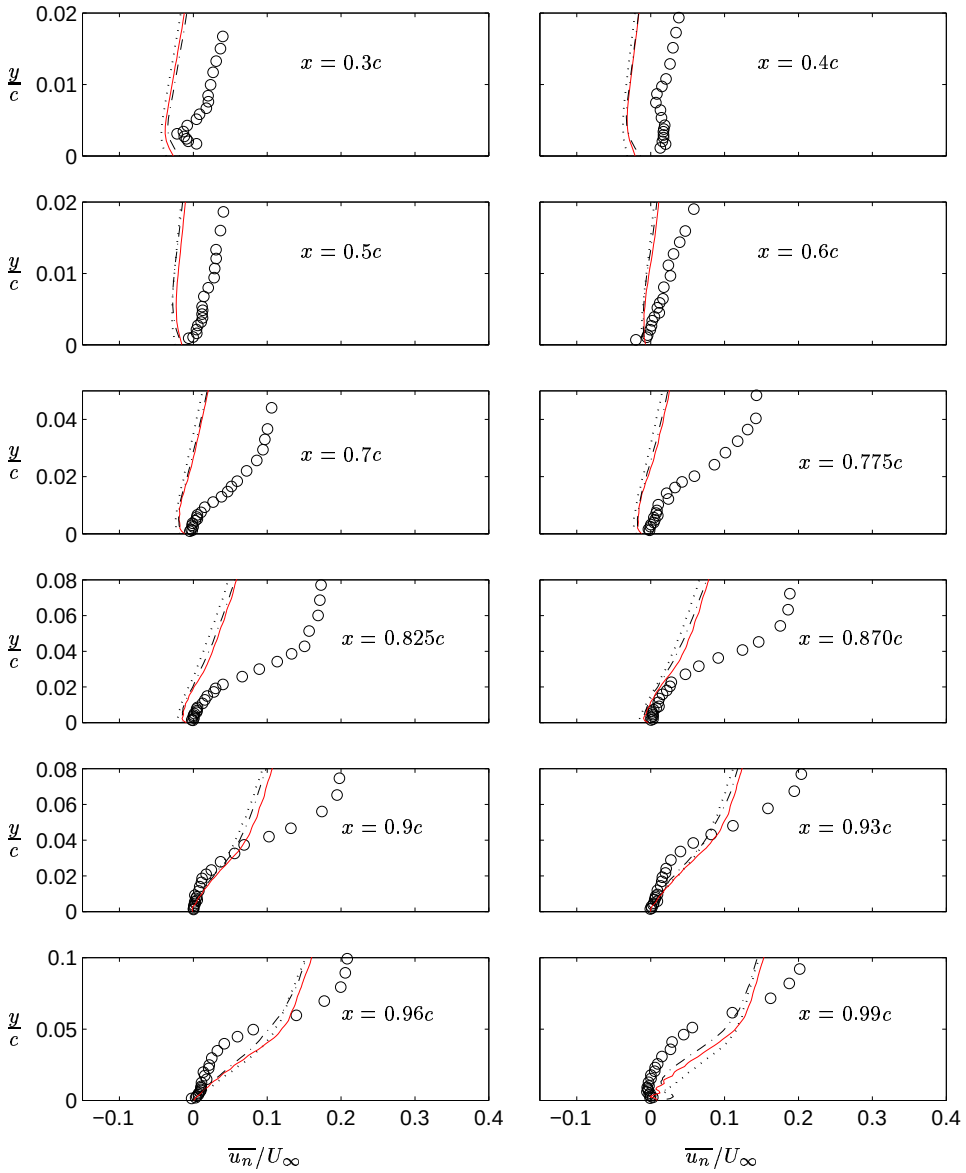

Figure 29: Spanwise and time averaged $\overline{u_n}$-velocity. Red solid: approximate wall boundary condition, Eqs. 35-37 (Comp. # 4); dotted: no-slip wall boundary condition (Comp. # 3); dash-dotted: upwinding scheme on the UMIST mesh (Comp. # 2); circles: exp. (F2). Subscripts s and n denote the directions parallel and normal to the airfoil wall, respectively.

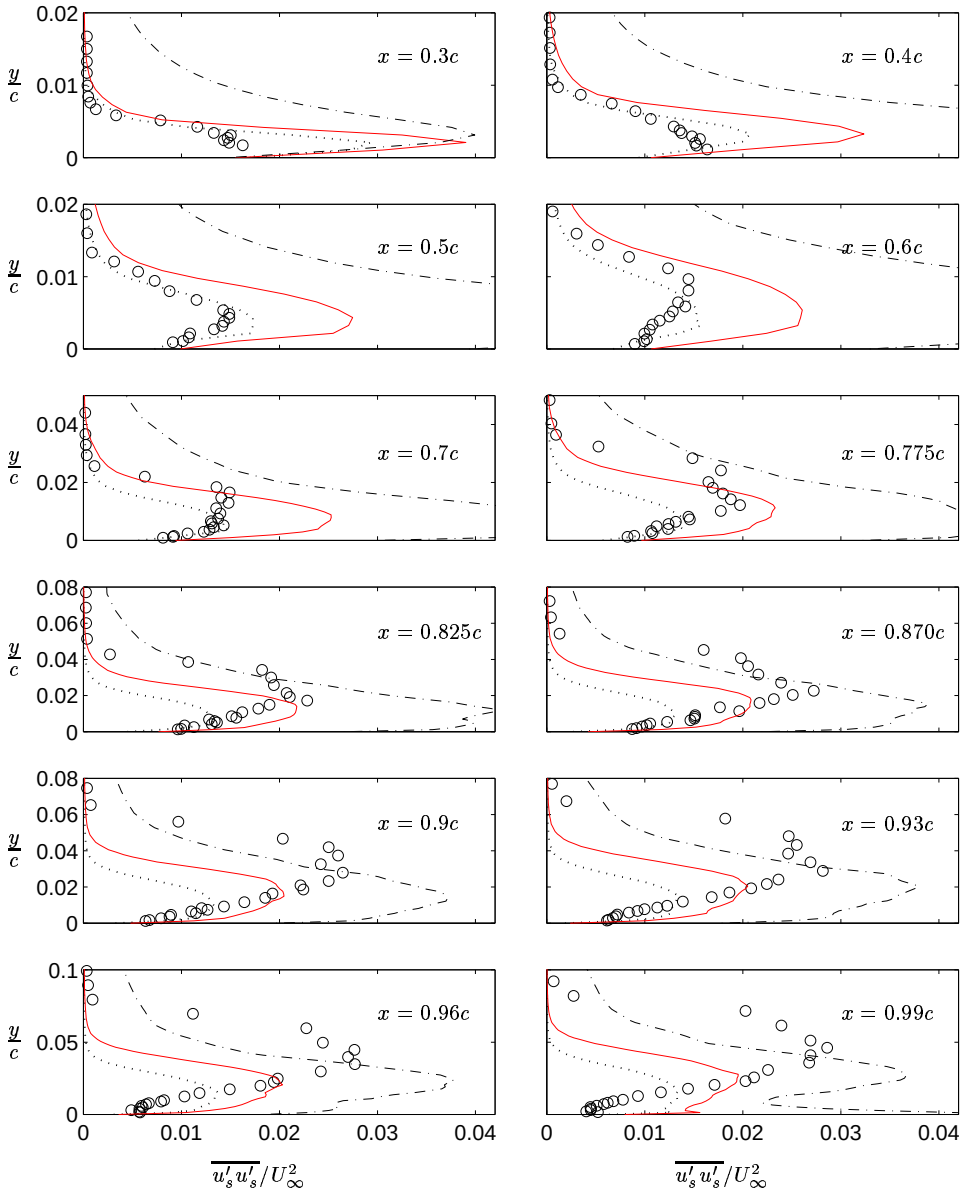

Figure 30: Spanwise and time averaged $\overline{u_s' u_s'}$-velocity. Red solid: approximate wall boundary condition, Eqs. 35-37 (Comp. # 4); dotted: no-slip wall boundary condition (Comp. # 3); dash-dotted: upwinding scheme on the UMIST mesh (Comp. # 2); circles: exp. (F2). Subscripts s and n denote the directions parallel and normal to the airfoil wall, respectively.

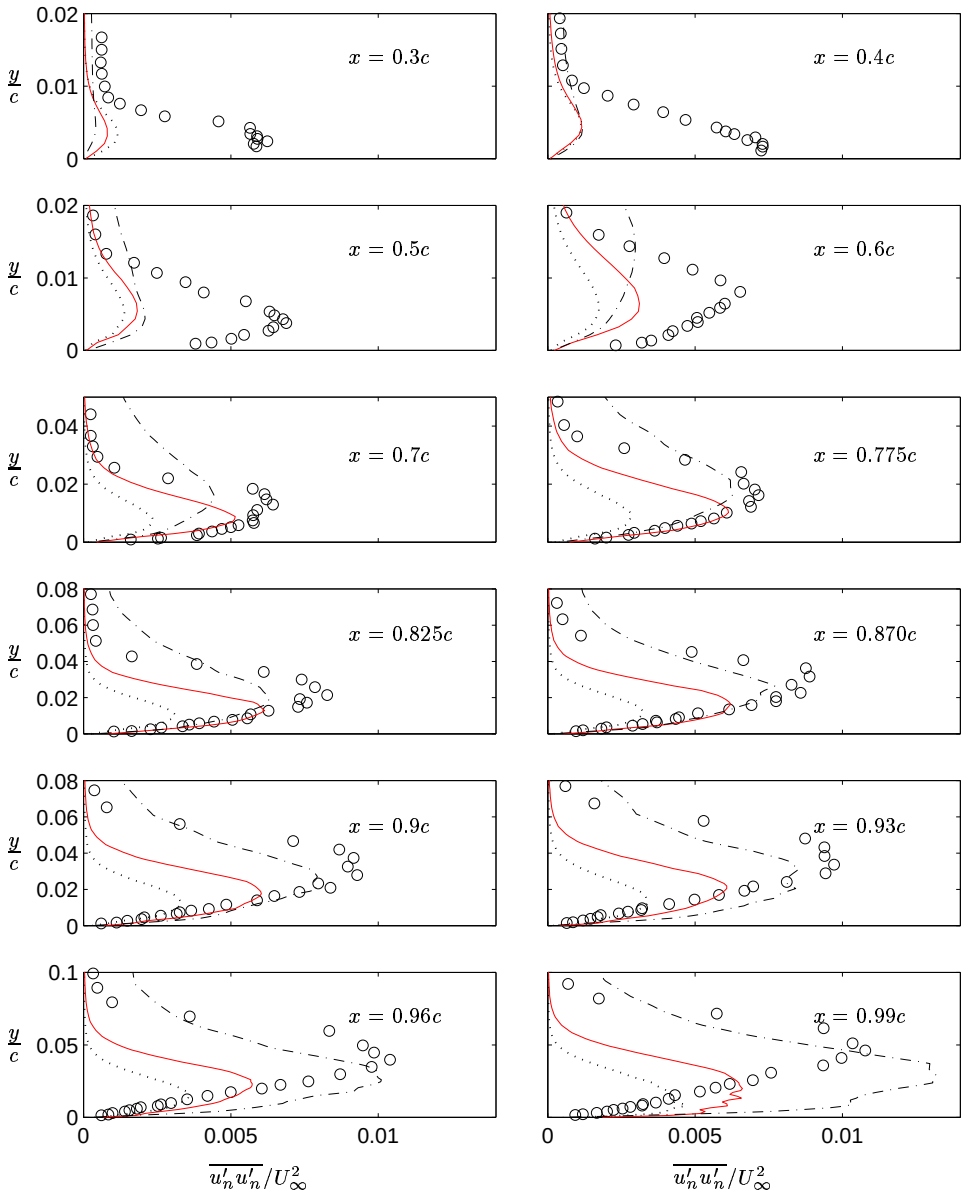

Figure 31: Spanwise and time averaged $\overline{u'_n u'_n}$-velocity. Red solid: approximate wall boundary condition, Eqs. 35-37 (Comp. # 4); dotted: no-slip wall boundary condition (Comp. # 3); dash-dotted: upwinding scheme on the UMIST mesh (Comp. # 2); circles: exp. (F2). Subscripts s and n denote the directions parallel and normal to the airfoil wall, respectively.

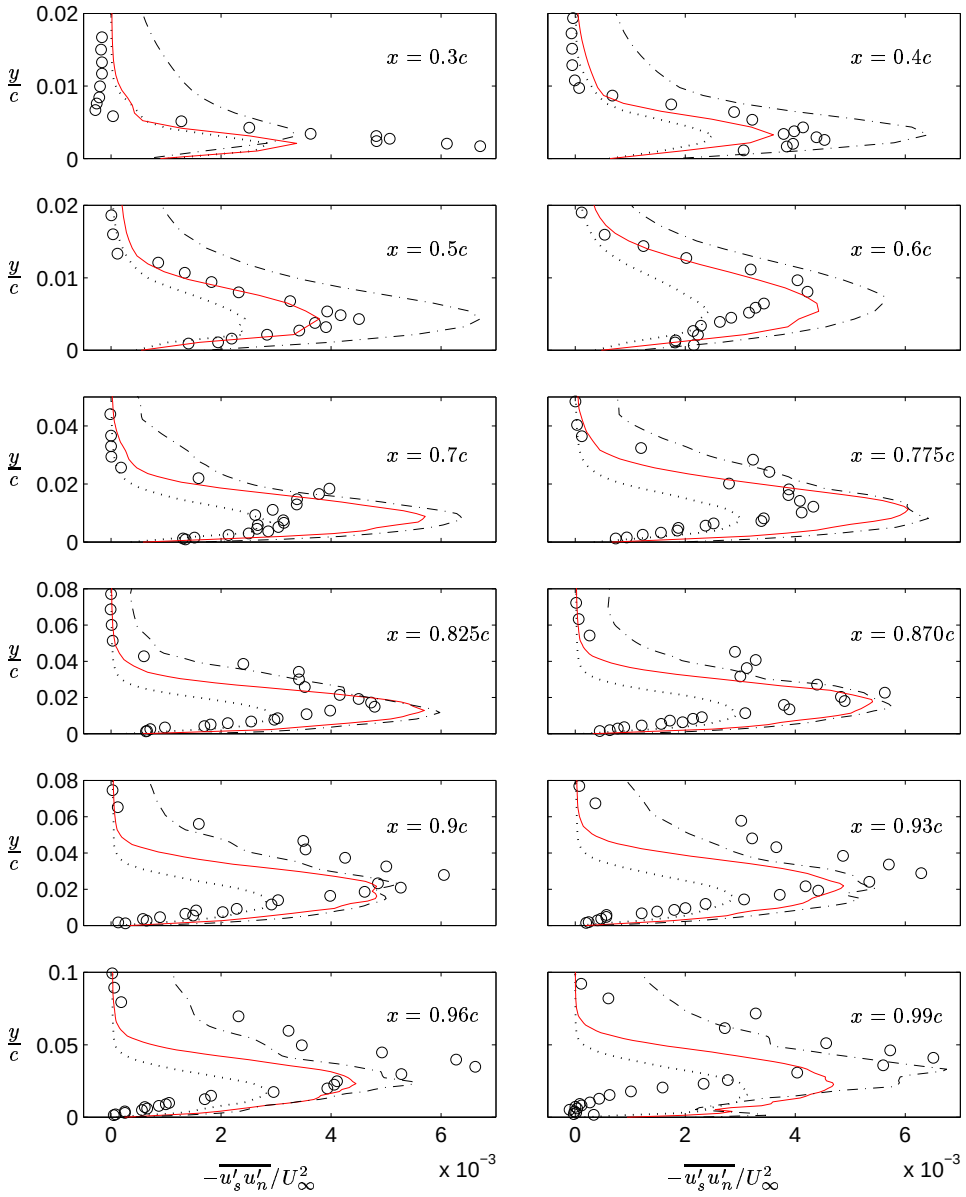

Figure 32: Spanwise and time averaged $\overline{u'_s u'_n}$-velocity. Red solid: approximate wall boundary condition, Eqs. 35-37 (Comp. # 4); dotted: no-slip wall boundary condition (Comp. # 3); dash-dotted: upwinding scheme on the UMIST mesh (Comp. # 2); circles: exp. (F2). Subscripts s and n denote the directions parallel and normal to the airfoil wall, respectively.

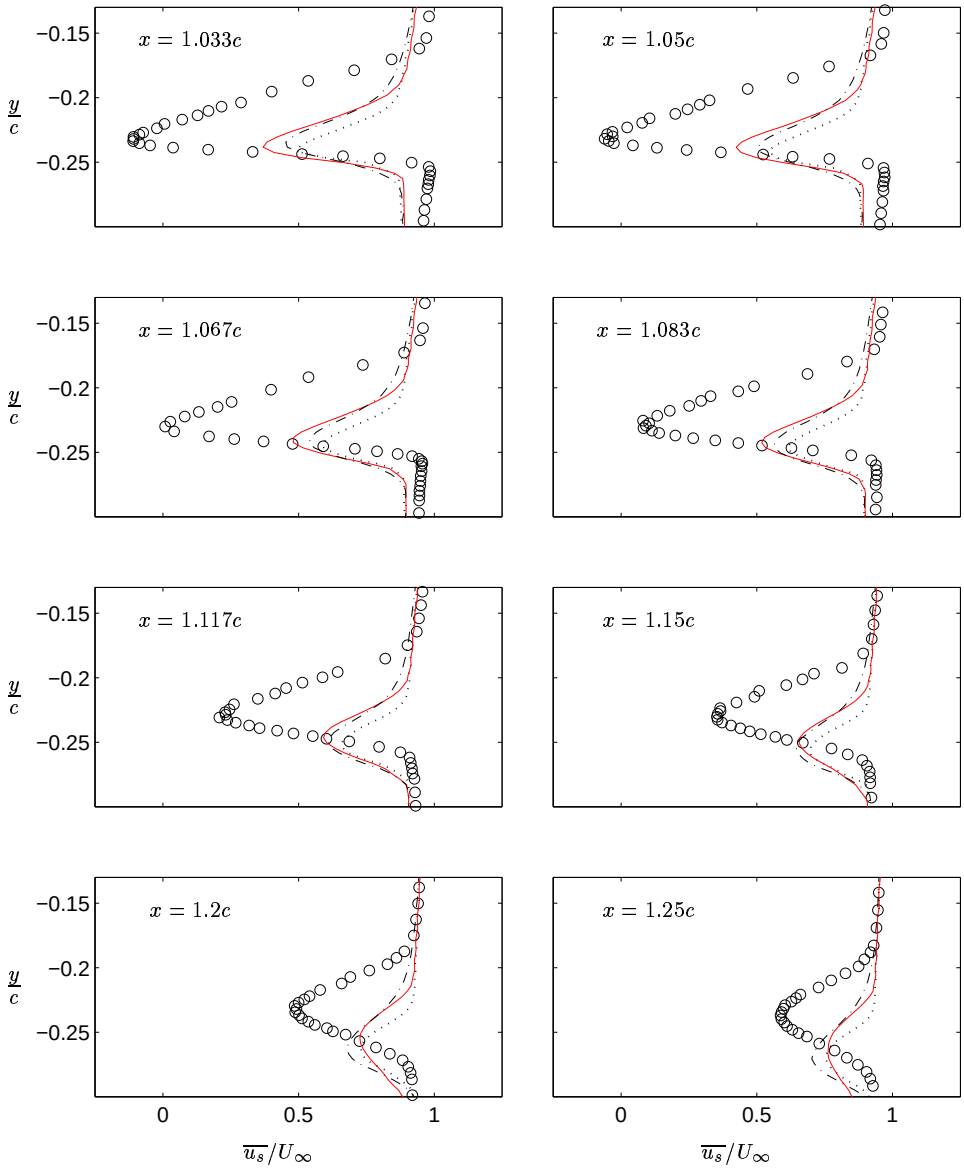

Figure 33: Spanwise and time averaged $\overline{u_s}$-velocity in the wake region. Red solid: approximate wall boundary condition, Eqs. 35-37 (Comp. # 4); dotted: no-slip wall boundary condition (Comp. # 3); dash-dotted: upwinding scheme on the UMIST mesh (Comp. # 2); circles: exp. (F2). Here the subscripts s and n denote the directions parallel and normal to the freestream velocity, respectively.

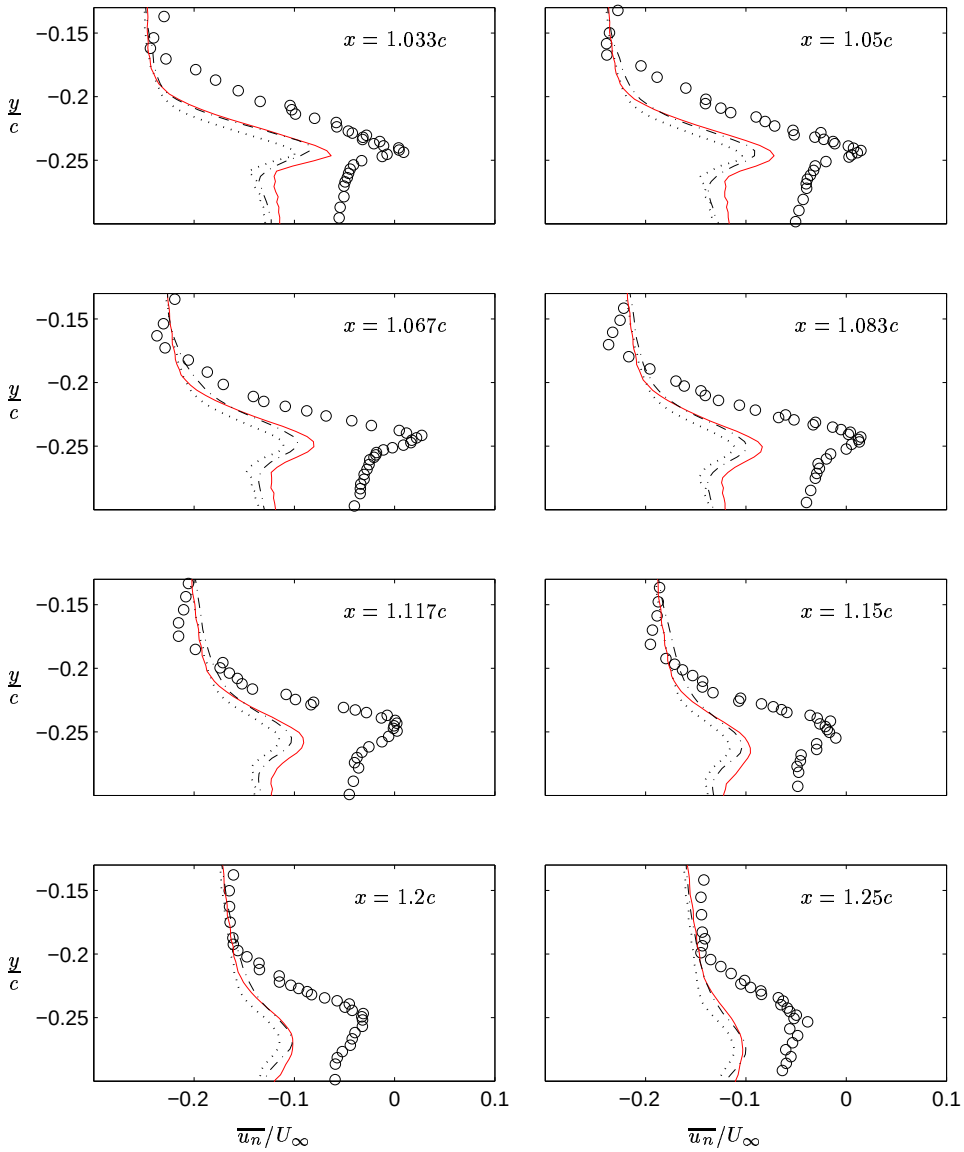

Figure 34: Spanwise and time averaged $\overline{u_n}$-velocity in the wake region. Red solid: approximate wall boundary condition, Eqs. 35-37 (Comp. # 4); dotted: no-slip wall boundary condition (Comp. # 3); dash-dotted: upwinding scheme on the UMIST mesh (Comp. # 2); circles: exp. (F2). Here the subscripts s and n denote the directions parallel and normal to the freestream velocity, respectively.

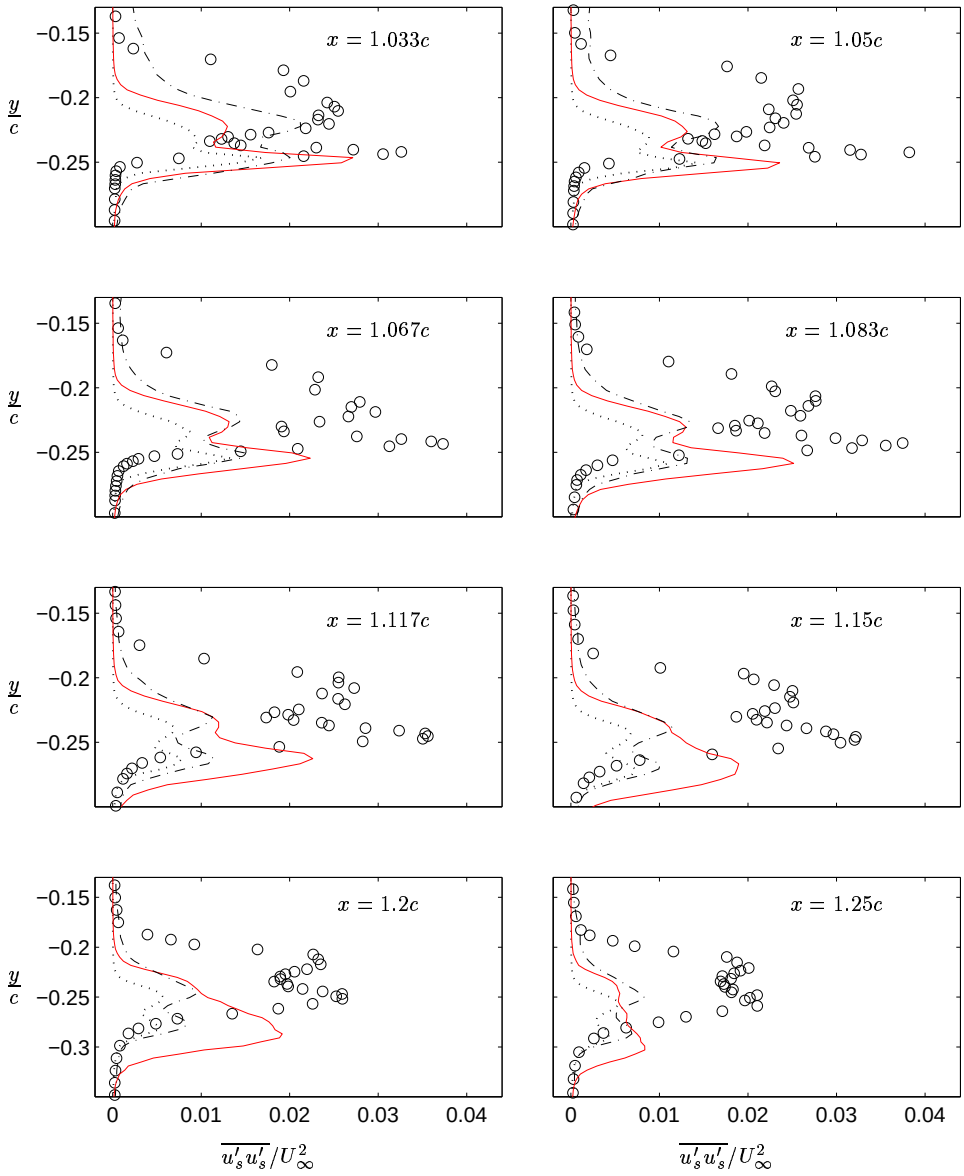

Figure 35: Spanwise and time averaged $\overline{u'_s u'_s}$-velocity in the wake region. Red solid: approximate wall boundary condition, Eqs. 35-37 (Comp. # 4); dotted: no-slip wall boundary condition (Comp. # 3); dash-dotted: upwinding scheme on the UMIST mesh (Comp. # 2); circles: exp. (F2). Here the subscripts s and n denote the directions parallel and normal to the freestream velocity, respectively.

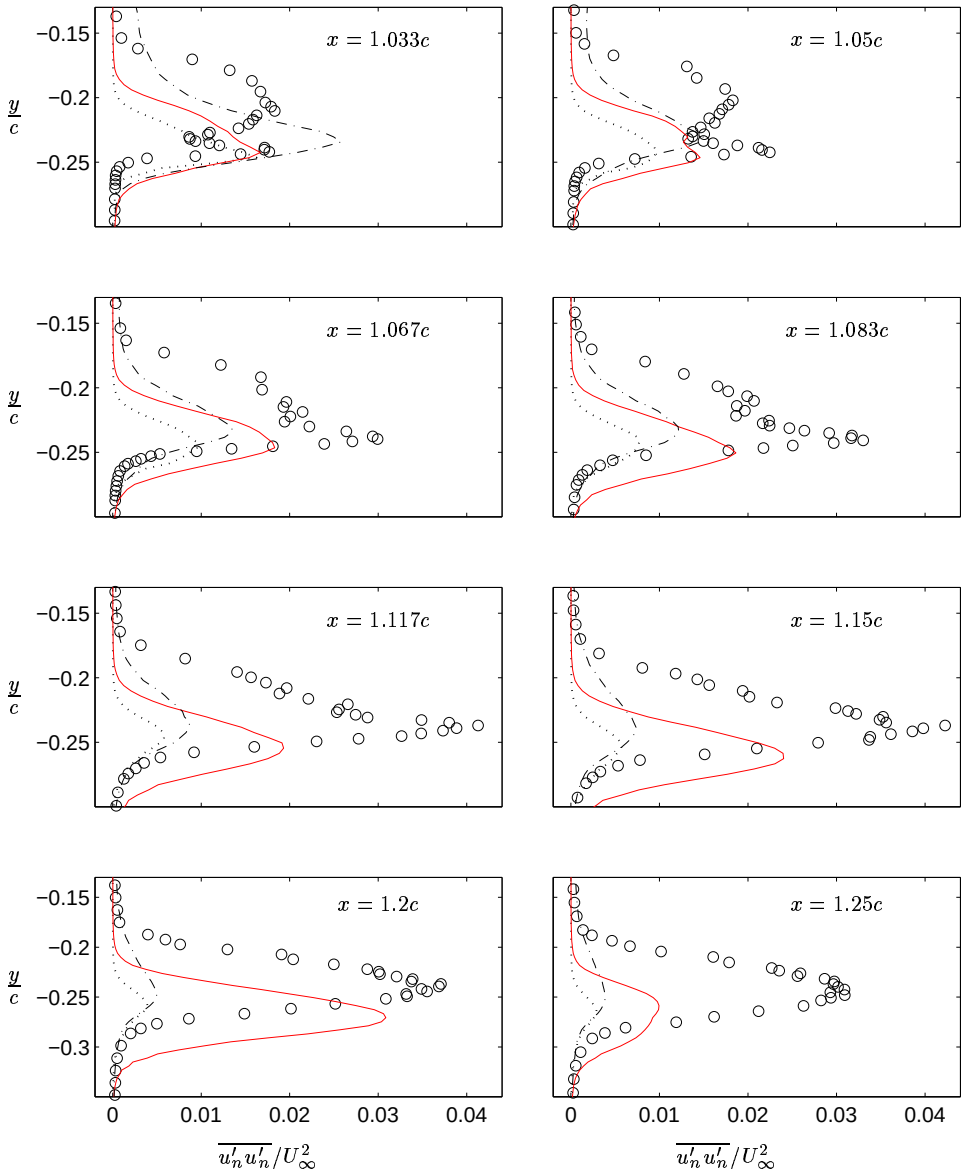

Figure 36: Spanwise and time averaged $\overline{u'_n u'_n}$-velocity in the wake region. Red solid: approximate wall boundary condition, Eqs. 35-37 (Comp. # 4); dotted: no-slip wall boundary condition (Comp. # 3); dash-dotted: upwinding scheme on the UMIST mesh (Comp. # 2); circles: exp. (F2). Here the subscripts s and n denote the directions parallel and normal to the freestream velocity, respectively.

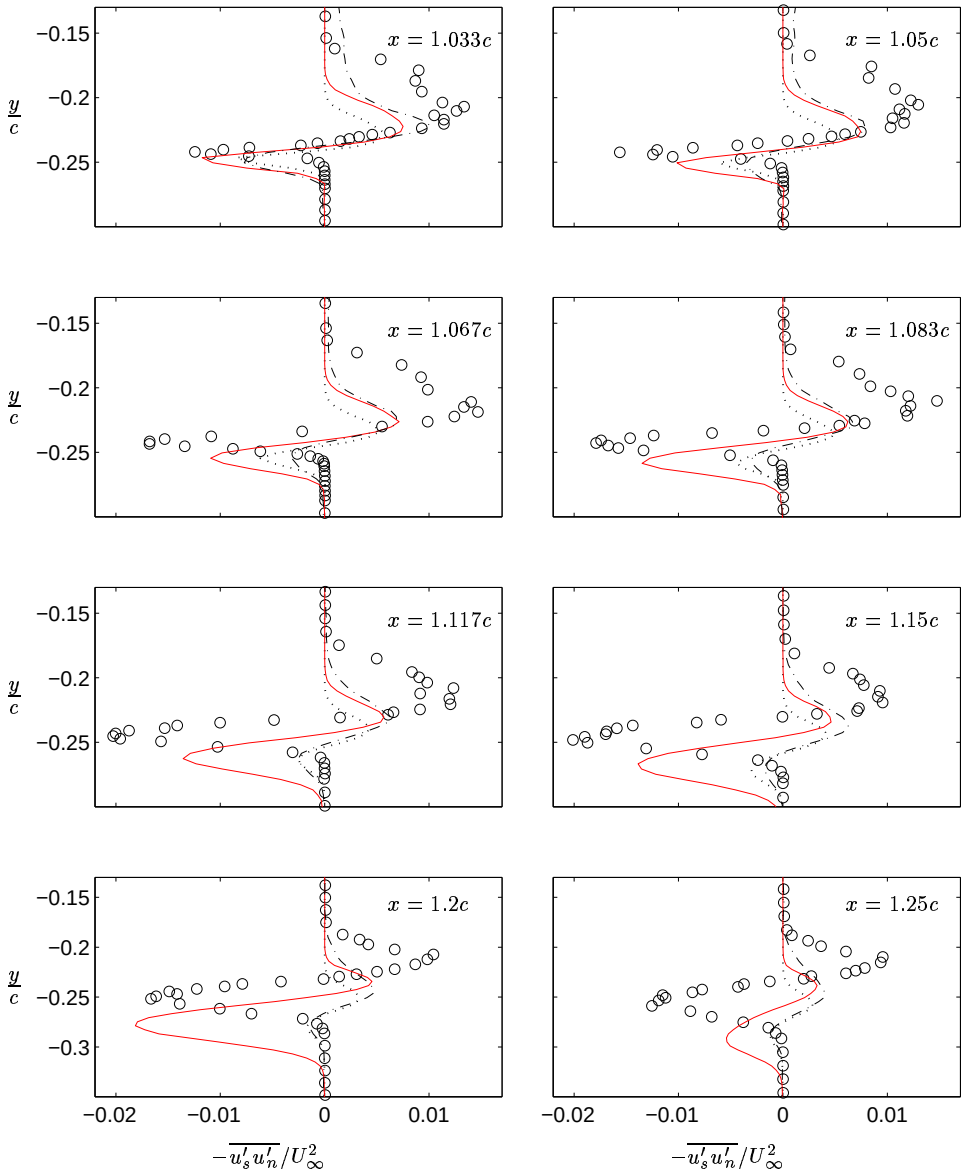

Figure 37: Spanwise and time averaged $\overline{u_s' u_n'}$-velocity in the wake region. Red solid: approximate wall boundary condition, Eqs. 35-37 (Comp. # 4); dotted: no-slip wall boundary condition (Comp. # 3); dash-dotted: upwinding scheme on the UMIST mesh (Comp. # 2); circles: exp. (F2). Here the subscripts s and n denote the directions parallel and normal to the freestream velocity, respectively.

on the overall results than the model in this case.

It is demonstrated in some RANS studies that the treatment of the transition has a major effect on the prediction of the trailing edge separation (see e.g. [29]). That is, the transition problem can spoil the validation of the performance of models.

Any conclusions about the feasibility of LES can probably not be drawn from these simulations, because of the far too coarse resolution in the laminar boundary layer.

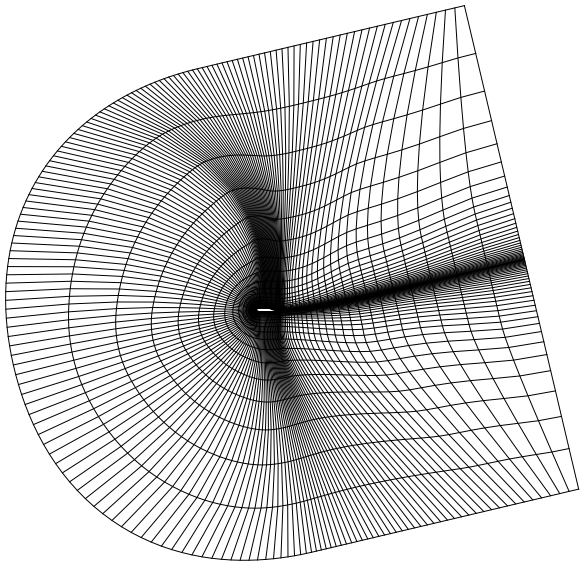

Figure 38: The Common mesh: 721×65 nodes (every 4th node in the i-direction and every 2nd node in the j-direction are plotted).

5.3 Further Details about the Meshes

Four computations on two different meshes were presented in the previous chapter. The second mesh, the Chalmers mesh, was generated in order to increase the resolution in the streamwise direction and to keep the stretching in this direction to a minimum. The Chalmers mesh is shown in more detail in Fig. 39, and contour plots of the stretching are shown in Fig. 40. The mesh was generated using *G2DMESH*, a 2D grid generator by Eriksson [30]. As is seen, the stretching is very low in the i-direction, the wrap-around direction around the airfoil. Especially, it

is less than 3% on the suction side of the airfoil. There is a region just downstream of the trailing edge where the stretching is higher than 5%. The stretching should of course preferably increase monotonically all the way to the outlet.

As mentioned in the conclusions in the previous chapter, the resolution was found to be inadequate in the separation region. For that reason a modified mesh was generated, the *Common* mesh (see Figs. 38 and 41). This new mesh consists of 721x65 grid nodes, one more in the i-direction in order also to be able to use a coarse version of this mesh with half the amount of nodes in the i-direction. In this mesh, the refinement downstream of the airfoil is even more aligned with the wake found in the computations performed. The main difference, as compared with the Chalmers mesh, is the resolution in the wall-normal direction. The wall resolution on the suction side of the airfoil is shown in Fig. 42

Mesh	**UMIST mesh**	**Chalmers mesh**	**Common mesh**
# of grid nodes:	321×65	720×65	721×65
# of nodes along the wake:	40	109	110
# of nodes on the pressure side:	121	201	200
# of nodes on the suction side:	121	302	302
Length of the cell at the leading edge:	$0.0012c$	$0.0010c$	$0.0010c$
Height of the cell at the leading edge:	$0.00025c$	$0.00026c$	$0.00026c$
Length of the cell at the trailing edge:	$0.0060c$	$0.0050c$	$0.0050c$
Height of the cell at the trailing edge:	$0.00049c$	$0.0028c$	$0.00049c$
Δx^+ in the separation region:	< 190	< 100	< 100
y^+ in the separation region:	< 4	< 30	< 5
# of cells within max. backflow at 0.99c:	7	1	7
# of cells in the laminar b.l. at the L.E.:	1	1	1
Maximum Δx^+ on the suction side:	1250	550	550
Maximum y^+ on the suction side:	20	40	19
Maximum aspect ratio:	132	48	70
Maximum i-stretching:	29.2%	5.9%	5.9%
Maximum j-stretching:	16.9%	20.7%	19.5%
Size of the computational domain:	$20c \times 20c$	$20c \times 20c$	$20c \times 20c$
Grid refinement along the wake:	no	yes	yes (more)

Table 4: Data on the UMIST mesh, the Chalmers mesh and the Common mesh.

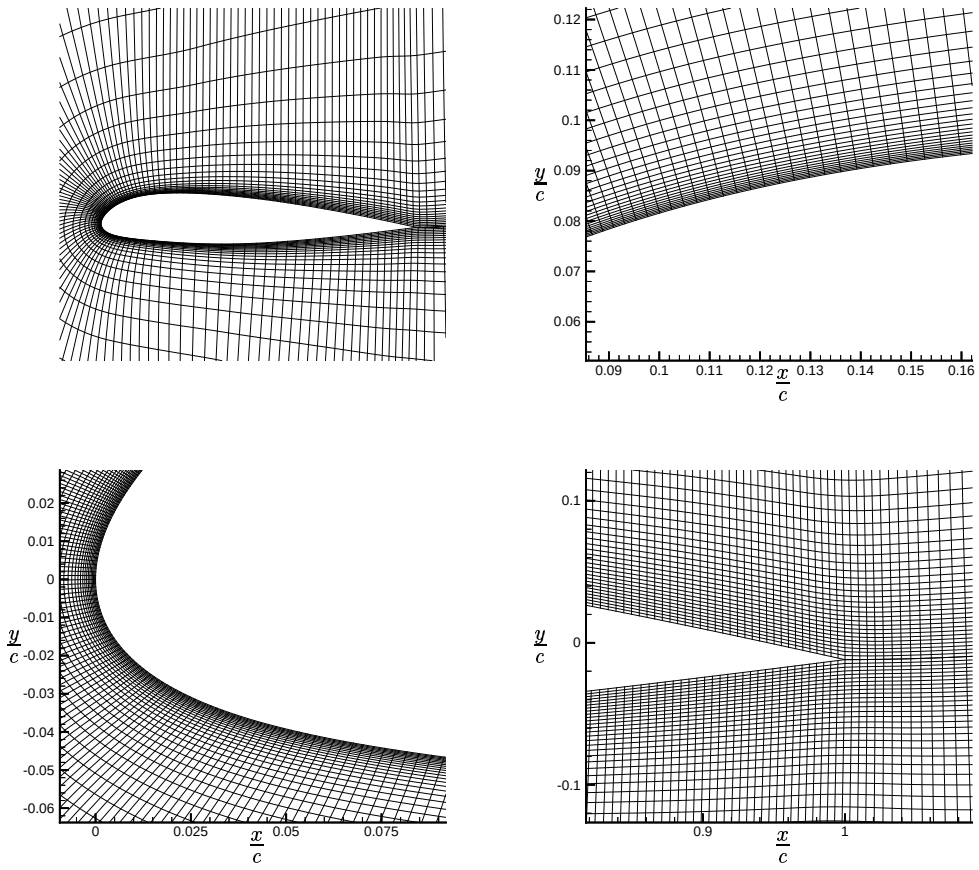

Figure 39: Zoom of the Chalmers mesh at the transition region and at the leading and trailing edges. Every 4th node in the i-direction and every 2nd node in the j-direction are plotted.

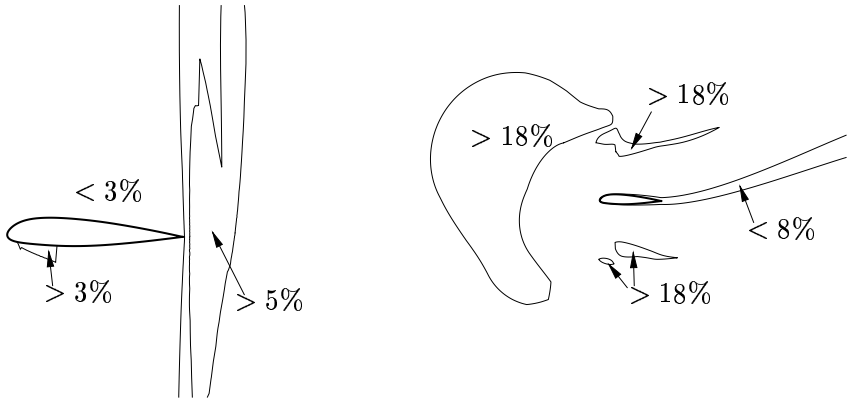

Figure 40: Stretching in the i-direction (left figure) and in the j-direction (right figure) on the Chalmers mesh.

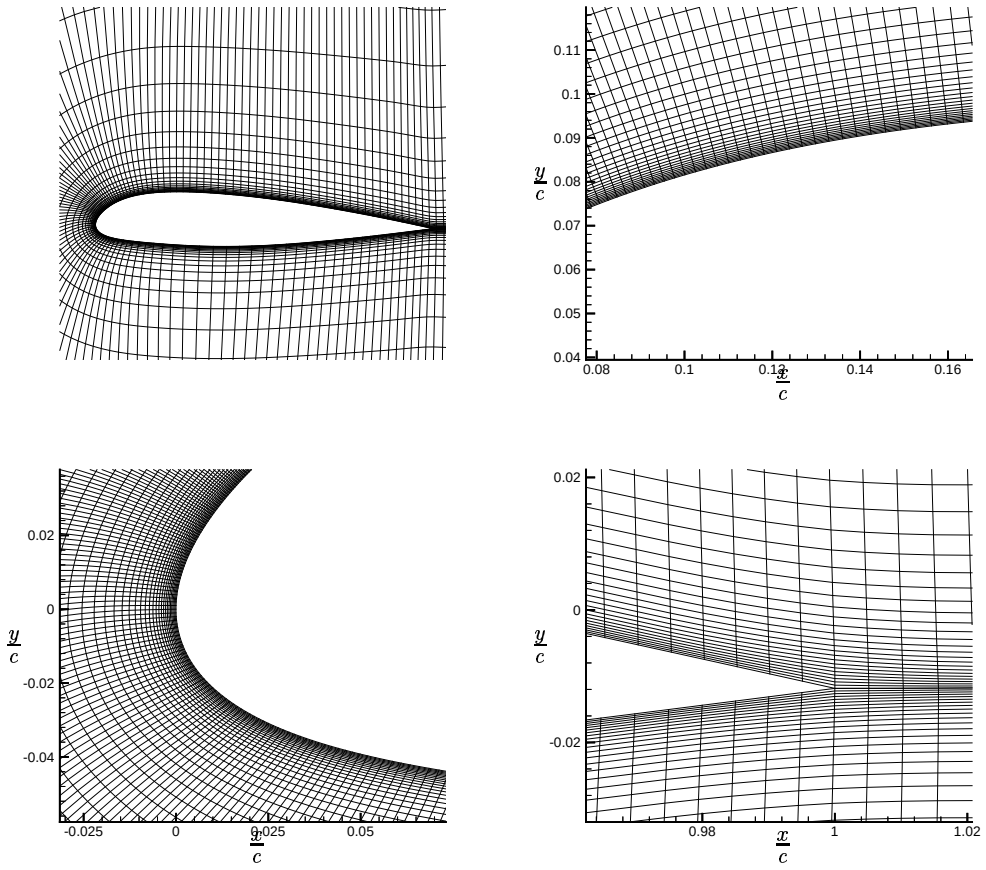

Figure 41: Zoom of the Common mesh at the transition region and at the leading and trailing edges. Every 4th node in the i-direction and every 2nd node in the j-direction are plotted.

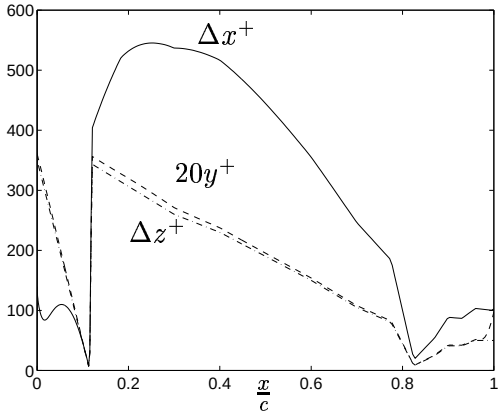

Figure 42: The size of the cell and the distance to the nearest node in dimensionless wall units along the suction side of the airfoil on the Common mesh ($L_z = 0.08c$).

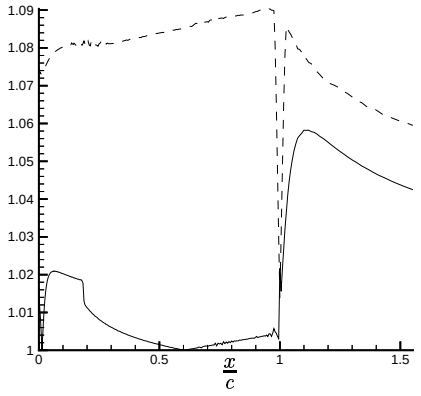

Figure 43: Stretching in the i-direction (solid line) and in the j-direction (dashed line) on the suction side of the airfoil and in parts of the wake on the Common mesh.

in the case when 33 nodes are used in the spanwise direction. Fig. 43 shows the stretching along the suction side. Data on this new mesh and the previous two are summarised in Table 4. Note that, also on this new mesh, the resolution of the laminar boundary layer is inadequate and the use of wall functions is necessary.

5.4 L^1- versus L^2-norm

Fig. 44 shows the p'-residual for computation #4 when the L^1- and the L^2-norms are used, respectively. The different computations are summarised in Table 2 at p. 25. For the velocities, the convergence criterion is that the L^1-norm of the residuals of the discretised momentum equations scaled with $\rho U_\infty A_{inlet} U_\infty$ should be less than the desired convergence level, η, where A_{inlet} is the projected area of the inlet. For the continuity equation, the criterion is that the L^1-norm of the discretised finite volume continuity error scaled with the inlet mass flow should be less than η.

For the computations on the UMIST mesh (Comp. # 1 and # 2), the convergence level is set to $1 \cdot 10^{-3}$. For Comp. # 3 and # 4, the scaled L^1-norm is approximately $1 \cdot 10^{-3}$ and sometimes exceeds the convergence level, η. Because of the very slow convergence within each time step, the approach of simply limiting the number of global iterations per time step is applied. For the computations on the Chalmers mesh, the number of iterations is set to two, corresponding to an η of approximately $1 \cdot 10^{-3}$. However, as seen in Fig. 44, the convergence criterion for the continuity equation is fulfilled for Comp. # 4. As an illustration, the L^2-norm of the error is plotted in the figure to the right. Of course, we

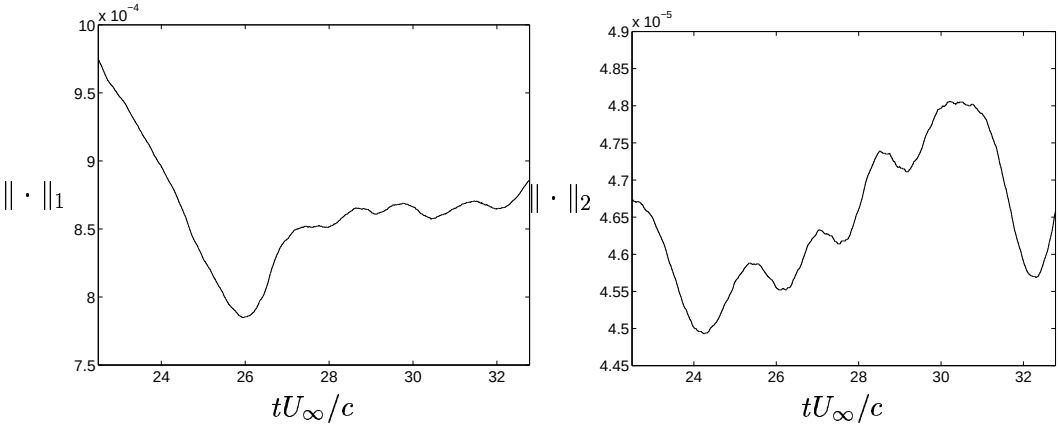

Figure 44: The L^1-norm (left figure) and the L^2-norm (right figure) of the integrated continuity error scaled with the inlet mass flow.

know not much more than that the following relation holds:

$$\|\cdot\|_\infty \leq \|\cdot\|_2 \leq \|\cdot\|_1 \tag{40}$$

and it is more restrictive to use the L^1-norm. For the present case, the L^2-norm is smaller by more than a factor of 10.

5.5 Mixed Schemes

Second order upwinding is used in parts of the domain to suppress odd-even oscillations. These wiggles are found mainly in the area around the leading edge. Unless they are suppressed, unphysical oscillations contaminate all of the computational domain. The convective terms for Comp. # 2-4 (see Table 2 at p. 25) are discretised so that the convective flux can be expressed as

$$\dot{m}u^m_{UDS} + \dot{m}\left[\alpha u^{m-1}_{CDS} - \alpha u^{m-1}_{UDS} + (1-\alpha)u^{m-1}_{UDScorr}\right] , \tag{41}$$

where CDS stands for the central difference scheme, UDS for the 1st-order upwind scheme and $UDScorr$ for the 2nd-order correction to the lower order upwind scheme ($m-1$ is the previous iteration). Here, α is a blending function ($0 \leq \alpha \leq 1$) and, at the extremes, we have

$\alpha = 0$: the van Leer scheme
$\alpha = 1$: the central difference scheme with deferred correction

The areas in which the CDS and the van Leer scheme are active and the mixing region between are shown in Fig. 45 for the computation on the UMIST mesh (Comp. # 2). The mixing region for Comps. # 3 and 4 is shown in Fig. 46. This blending function was chosen in order to more accurately prescribe the transition, as in the experiments. The Smagorinsky eddy viscosity was also mixed (see Fig. 46) but, as discussed in the previous chapter, probably too far downstream.

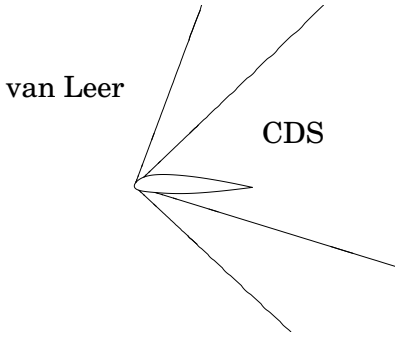

Figure 45: Blending function used for the schemes in Comp. # 2.

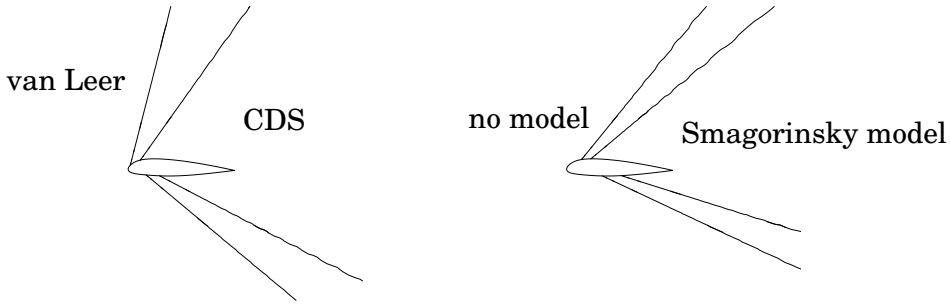

Figure 46: Blending functions used for the schemes (left figure) and for the SGS model (right figure) in Comp. # 3 and # 4.

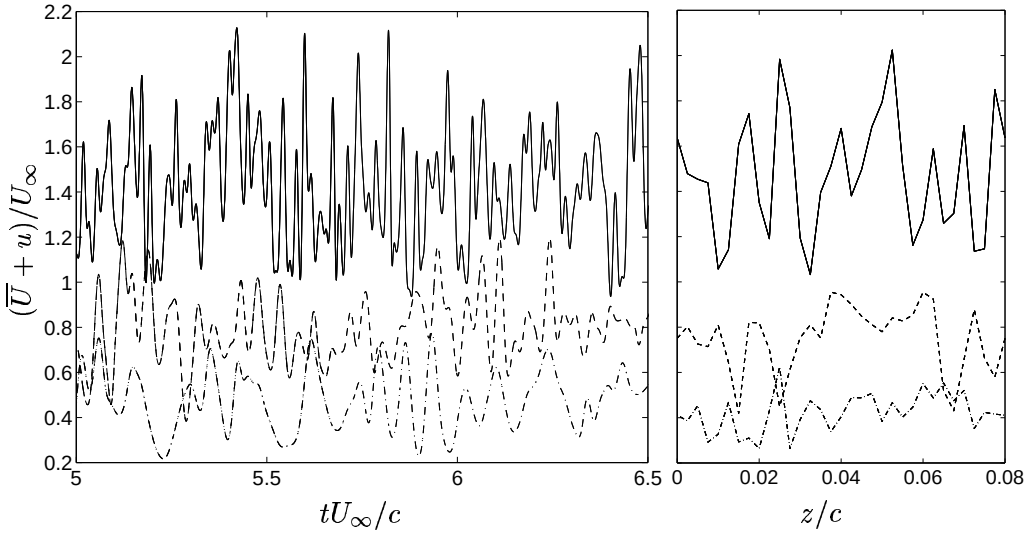

Figure 47: Resolved velocity in the streamwise direction at approximately 12% of the boundary layer ($y/\delta \approx 0.12$). A segment of the signal is plotted in the left figure, and the signal in space (the spanwise direction) is plotted at an instant in the right figure. Solid: $x = 0.2c$; dashed $x = 0.6c$; dash-dotted: $x = 0.9c$.

6 A Short Analysis of the Turbulence in a High Reynolds Large Eddy Simulation

6.1 Introduction

In Large Eddy Simulations (LES), the contributions of the small scales are modeled using a subgrid scale (SGS) model. The main task of the model is to dissipate the correct amount of energy from the resolved scales (down to the small scales). The present Smagorinsky model (and many other SGS models) is based on the assumption that the smallest resolved scales are isotropic. With an anisotropic mean flow, the smallest resolved scales need at least be in the Kolmogorov -5/3-range (the inertial subrange) where local isotropy might be expected.

What information can we get from the resolved or large scale variables in a LES? Especially, looking at the present simulation, do the resolved variables model the physics of the resolved scale turbulence in a correct way? Which are the scales that are resolved? From the resolved scales, is it possible to obtain a good estimate of the smallest scales in the turbulence, the Kolmogorov scales? Indeed, this is the role of the SGS model, but how well does the model predict those scales? Also, is it possible to estimate the largest scales, especially can any conclusions

be drawn about whether the spanwise extent is sufficient? These issues are discussed in this section.

Turbulence is chaotic and contains a range of scales. Thus, statistical methods and spectral analysis are helpful tools when studying the phenomenon. In the following subsections, some of the tools are described and applied to the present simulation (Comp. # 4) and compared with the theory of energy spectra and scale relations in order to try to 'answer' the questions above.

6.2 Turbulent LES Signals

The data are collected for the resolved velocities at three different locations along the suction side of the airfoil, at $x/c = 0.20$ (a small distance downstream of the transition), at $x/c = 0.60$ and at $x/c = 0.9$. The data are 'measured' (in time and in the spanwise direction) in the turbulent boundary layer at the fourth node from the wall. Fig. 47 shows the 'signals' in time and space for the resolved velocity in the x-direction.

The boundary layer is under the influence of curvature and an adverse pressure gradient. The locations are summarised in Table 5, also including the Reynolds number based on the boundary layer thickness and velocity, Re_δ, as well as some statistics of the resolved velocities. The non-dimensional pressure gradient parameter, $K = \frac{-\nu}{\rho U_\infty^3}\frac{\partial \bar{p}}{\partial x}$, is also shown. Throughout this section we let the bar denote time averaging (not filtering) and let u_i denote the velocity fluctuation in the x_i-direction, regardless of whether the signal is a real turbulent signal or a filtered LES signal. The mean value of the signal is denoted by $\overline{U_i}$. There is no summation on subsubindexes. Although the time averaging

x/c	y^+	$K \cdot 10^6$	δ/c	Re_δ
0.20	180	-2.4	0.01	$3.6 \cdot 10^4$
0.60	320	-0.55	0.04	$1.0 \cdot 10^5$
0.90	320	-0.41	0.07	$1.4 \cdot 10^5$

x/c	$\overline{uu}/U_\infty^2$	$\overline{vv}/U_\infty^2$	$\overline{ww}/U_\infty^2$	$\overline{U}/U_\infty$	$\overline{V}/U_\infty$	$\overline{W}/U_\infty$
0.20	$6.8 \cdot 10^{-2}$	$7.8 \cdot 10^{-3}$	$9.1 \cdot 10^{-3}$	1.4	0.070	$9.7 \cdot 10^{-4}$
0.60	$2.4 \cdot 10^{-2}$	$4.5 \cdot 10^{-3}$	$8.0 \cdot 10^{-3}$	0.77	-0.12	$-7.4 \cdot 10^{-4}$
0.90	$1.6 \cdot 10^{-2}$	$6.3 \cdot 10^{-3}$	$6.6 \cdot 10^{-3}$	0.46	-0.084	$12.0 \cdot 10^{-4}$

Table 5: Data in the turbulent boundary layer at a wall distance of $y/\delta \approx 0.12$.

is quite long ($T_{ave} = 10c/U_\infty$), we note that the resolved velocity in the spanwise direction is not quite equal to zero (which it should be in this symmetric flow).

The method and computational set-up used for the simulation analysed (Comp. # 4) are described in more detail in Chapter 4. Here we merely mention the sampling 'frequencies'. The time step, Δt, is equal to $3 \cdot 10^{-4}$ and the spatial resolutions at the three locations are shown in Table 6 (x is approximately the streamwise direction, y is approximately the wall normal direction and z is the spanwise direction).

$\mathbf{x/c}$	$\Delta x/c$	Δx^+	$\Delta y/c$	Δy^+	$\Delta z/c$	Δz^+
0.20	$4.3 \cdot 10^{-3}$	600	$3.8 \cdot 10^{-4}$	53	$2.5 \cdot 10^{-3}$	347
0.60	$5.9 \cdot 10^{-3}$	380	$1.4 \cdot 10^{-3}$	94	$2.5 \cdot 10^{-3}$	162
0.90	$5.3 \cdot 10^{-3}$	220	$2.3 \cdot 10^{-3}$	96	$2.5 \cdot 10^{-3}$	104

Table 6: Resolution in the turbulent boundary layer at $y/\delta \approx 0.12$.

6.3 Correlation

Turbulence is often characterized as random. However, when looking at a turbulent signal in time or space, the velocity fluctuations at two points a certain distance apart might be *correlated* to each other, i.e. the time averaged product between the fluctuations might be nonzero. In space, given a stationary velocity field, the correlation tensor, $R_{u_i u_j}$, is given by

$$R_{u_i u_j}(\mathbf{r}) = \overline{u_i(\mathbf{x}) u_j(\mathbf{x}+\mathbf{r})} \; . \tag{42}$$

At a given correlation distance, $\mathbf{r}$, $R_{u_i u_j}(\mathbf{r})$ is the two-point correlation between the fluctuations u_i and u_j. In the literature, this correlation is sometimes normalised with the stress $\overline{u_i u_j(\mathrm{x})}$ or with $u_i'(\mathrm{x}) u_j'(\mathrm{x}+\mathrm{r})$ if $\mathbf{r}$ is in an inhomogeneous direction, where u' is the rms value ($u' = \sqrt{\overline{u^2}}$). Correlations in the spanwise direction, $R_{u_i u_i}(z)$ are shown in Fig. 48 at the three locations in the boundary layer described above.

6.3.1 Integral scales

Correlation curves give information about the range of scales present in turbulent flow. One measure of the correlation is the *integral scale*, $L_{u_i u_j}$, defined as

$$L_{u_i u_j} = \frac{1}{\overline{u_i u_j}} \int_0^\infty R_{u_i u_j}(\mathbf{r}) d\mathrm{r} \; . \tag{43}$$

For the example in our case, we have (in the spanwise direction) the *longitudinal* integral scale $L^z_{ww} = \frac{1}{\overline{ww}} \int_0^\infty R_{ww}(z) dz$ and the *transverse* integral scales, L^z_{uu} and L^z_{vv}. It is clearly seen in the figures that the integral scales become larger as the boundary layer thickens.

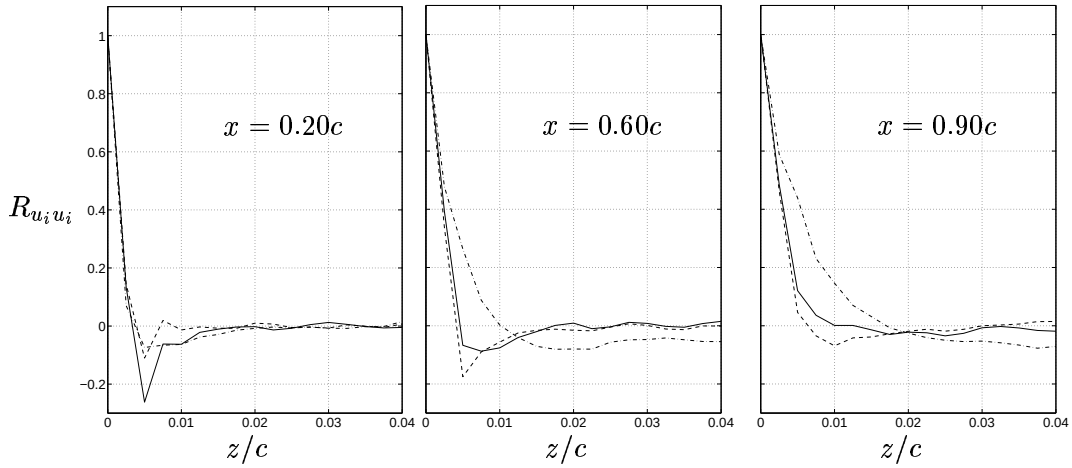

Figure 48: Spanwise autocorrelations (normalised) of the resolved velocities at approximately 12% of the boundary layer. Solid: R_{uu}; dashed R_{vv}; dash-dotted: R_{ww}.

Computed integral scales are shown in Table 7 (integrated from zero to $L_z/2$). The scales become larger with increasing boundary layer thick-

$\mathbf{x/c}$	L^z_{uu}/c	L^z_{vv}/c	L^z_{ww}/c
0.20	$0.50 \cdot 10^{-3}$	$1.3 \cdot 10^{-3}$	$0.63 \cdot 10^{-3}$
0.60	$1.6 \cdot 10^{-3}$	$1.0 \cdot 10^{-3}$	$1.6 \cdot 10^{-3}$
0.90	$2.4 \cdot 10^{-3}$	$1.9 \cdot 10^{-3}$	$3.8 \cdot 10^{-3}$

Table 7: Longitudinal and transverse integral scales in the spanwise direction at $y/\delta \approx 0.12$.

ness (this is not seen in the integral scale L^z_{vv}, but note that R^z_{vv} does not stay negative for a long distance and there is not much negative contribution to the integral scale). The integral scales are a measure of relatively large scales, but they are not appropriate length scales for the largest structures in the turbulence for most of these curves, where the correlations become negative on a wide range of correlation distances. A more appropriate estimate of the largest scales would be the correlation distance, z^*, for which $R_{u_iu_i}(z > z^*) \approx 0$. Judging from this subjective condition, it is seen that scales are present that are larger than the boundary layer thickness and also, at $x = 0.6c$ and $x = 0.9c$, of the size of the spanwise extent, L_z, which might be a reason for increasing this extension.

6.3.2 Microscales

If the Reynolds number is high enough, *microscales* exist in the equilibrium range.

If the r-direction is a homogeneous direction, we note that $R_{u_i u_j}(r)$ is symmetric around $r = 0$. It can be shown that the curvature of autocorrelation, $R_{u_i u_i}$, at $r = 0$ is related to correlations of derivatives of velocities. In fact, in the case of homogeneous turbulence in all directions, i.e. isotropic turbulence, it can be shown that all terms in the dissipation term, $\epsilon = 2\nu\overline{s_{ij}s_{ij}}$, can be related to the curvature of the longitudinal correlation at $r = 0$ (see Hinze [32]). Introducing the *longitudinal microscale* in the z-direction (and likewise in the other directions), λ^z_{ww}, as

$$\overline{\left[\frac{\partial w}{\partial z}\right]^2_{z=0}} = \frac{2w'^2}{(\lambda^z_{ww})^2} \tag{44}$$

and the *transverse microscales*, λ^z_{uu} and λ^z_{vv} as

$$\overline{\left[\frac{\partial u}{\partial z}\right]^2_{z=0}} = \frac{2u'^2}{(\lambda^z_{uu})^2} \tag{45}$$

$$\overline{\left[\frac{\partial v}{\partial z}\right]^2_{z=0}} = \frac{2v'^2}{(\lambda^z_{vv})^2}\,, \tag{46}$$

we have that

$$\begin{aligned}
\frac{1}{(\lambda^z_{ww})^2} &= -\frac{1}{2w'^2}\left[\frac{\partial^2 R_{ww}}{\partial z^2}\right]_{z=0} \\
\frac{1}{(\lambda^z_{uu})^2} &= -\frac{1}{2u'^2}\left[\frac{\partial^2 R_{uu}}{\partial z^2}\right]_{z=0} \\
\frac{1}{(\lambda^z_{vv})^2} &= -\frac{1}{2v'^2}\left[\frac{\partial^2 R_{vv}}{\partial z^2}\right]_{z=0}
\end{aligned} \tag{47}$$

Although the resolution around zero correlation ($z = 0$) is coarse, it can be seen that the correlation curves go steeply toward zero, indicating microscales in the order of the grid resolution ($\Delta z = 0.0025$). Especially at $x = 0.2c$, the curves indicate microscales perhaps less than the grid resolution. Perhaps a major part of these scales are not resolved at all near the transition. From the relation for the dissipation, the microscales could be seen as the average size of the eddies that are mainly responsible for the dissipation. In LES, it might be important to resolve these scales.

Altogether, the present correlation curves indicate a large spectrum of scales, larger than the resolved spectrum. At 20% of the chord, the

spanwise extent is (more than) sufficient, but the eddies of the microscale size are not well resolved. Further downstream, these eddies become more and more resolved but, at the same time, the largest scales become more and more restricted by the spanwise extension. Perhaps the spanwise extension is insufficient.

6.4 Energy spectra

Taking the Fourier transform of the correlations, i.e. looking at the correlations in the Fourier (wave number) space, gives additional information on the turbulence. Through Parseval's relation it is found that the spectrum is the energy content for u_i' at different length scales (see e.g. Tennekes and Lumley [11]). The spectrum is defined in such a way that the integral of the Fourier transformed correlation is equal to $u_i'^2$.

It could be defined in the inverse wave length space, $\lambda^{-1} > 0$, as

$$\tilde{E}_{u_iu_i}(\lambda^{-1}) = 2\int_{-\infty}^{\infty} R_{u_iu_i}(r)e^{-i2\pi\lambda^{-1}r}dr \ , \tag{48}$$

where the factor 2 comes from the definition that $\int_{-\infty}^{\infty}\tilde{E}_{u_iu_i}d\lambda^{-1} = u_i'^2$. However, it is customary to define it in the wave number space, $k > 0$, as

$$E_{u_iu_i}(k) = \frac{\tilde{E}_{u_iu_i}(\lambda^{-1})}{2\pi} = \frac{1}{\pi}\int_{-\infty}^{\infty} R_{u_iu_i}(r)e^{-ikr}dr \ . \tag{49}$$

The wave number, k, is related to the wave length, λ, as $k = 2\pi\lambda^{-1}$. k corresponds to the angular frequency, ω, when looking at frequency spectra and λ^{-1} corresponds to the frequency, f.

If r is in a homogeneous direction, then $R_{u_iu_i}$ is symmetric, the Fourier transform real and symmetric and we can write:

$$E_{u_iu_i}(k) = \frac{1}{\pi}\int_{-\infty}^{\infty} R_{u_iu_i}(r)e^{-ikr}dr =$$
$$\frac{1}{\pi}\int_{-\infty}^{\infty} R_{u_iu_i}(r)coskrdr = \frac{2}{\pi}\int_{0}^{\infty} R_{u_iu_i}(r)coskrdr \ . \tag{50}$$

In the present case the spanwise direction is homogeneous and $R_{u_iu_j}(z) = R_{u_iu_j}(-z)$. Approximations (using fast Fourier transforms) of these one dimensional energy spectra are plotted in Fig. 49. The inverse Fourier transform (if $R_{u_iu_i}$ is symmetric) is given by

$$R_{u_iu_i}(r) = \int_{0}^{\infty} E_{u_iu_i}(k)coskrdk \ . \tag{51}$$

Although not plotted in the figures, the spectra at wave number 0 are proportional to the integral scales, because, from Eq. 50, we have

$$\lim_{k\to 0} E_{u_iu_i}(k) = \frac{2}{\pi}\int_{0}^{\infty} R_{u_iu_i}(r)dr = \frac{2u_i'^2}{\pi}L_{u_iu_i} \ . \tag{52}$$

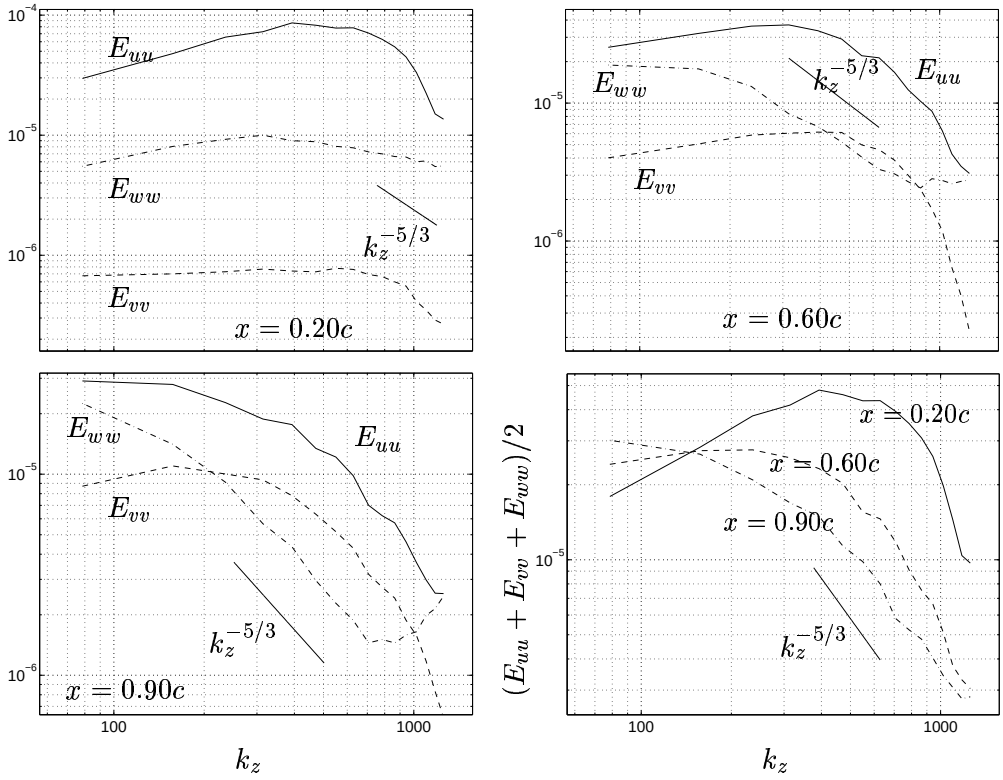

Figure 49: Spanwise one dimensional energy spectra of the resolved velocities at $y/\delta \approx 0.12$.

By differentiating Eq. 51 twice, and, together with the relations for the micro scales (Eqs. 47), we have

$$\frac{1}{(\lambda^r_{u_i u_i})^2} = -\frac{1}{2u_i'^2}\left[\frac{\partial^2 R_{u_i u_i}}{\partial r^2}\right]_{r=0} = \frac{1}{2u_i'^2}\int_0^\infty k^2 E_{u_i u_i}(k)dk \ . \tag{53}$$

With this expression, it is clearly seen that the micro scales depend on the high wave numbers and that estimates integrating over the resolved scales from the approximate energy spectra would result in overpredicted values. Table 8 shows the estimated microscales.

$\mathbf{x/c}$	λ^z_{uu}/c	λ^z_{vv}/c	λ^z_{ww}/c
0.20	$0.89 \cdot 10^{-3}$	$0.88 \cdot 10^{-3}$	$0.82 \cdot 10^{-3}$
0.60	$1.1 \cdot 10^{-3}$	$1.1 \cdot 10^{-3}$	$1.1 \cdot 10^{-3}$
0.90	$1.2 \cdot 10^{-3}$	$1.2 \cdot 10^{-3}$	$1.2 \cdot 10^{-3}$

Table 8: Longitudinal and transverse microscales in the spanwise direction at $y/\delta \approx 0.12$.

In many ways we get the same information concerning the spectrum of scales as we get from the correlation curves, although more apparent in the energy spectra. In the figure in which the kinetic energy spectra are plotted at the different x-locations (see Fig. 49), it is clearly seen that the 'LES window' moves from larger scales to smaller scales the farther downstream in the boundary layer we look. The window covers smaller scales but perhaps misses (suppresses) the largest.

6.4.1 Frequency spectra

Defining the autocorrelation in time

$$R_{u_iu_j}(t) = \overline{u_i(\tau)u_j(\tau - t)} \; , \tag{54}$$

we have the frequency energy spectrum (corresponding to $\tilde{E}_{u_iu_i}$ in Eq.48)

$$E_{u_iu_i}(f) = 4\int_0^\infty R_{u_iu_i}(t) cos 2\pi f t dt \tag{55}$$

and its inverse Fourier transform

$$R_{u_iu_i}(t) = \int_0^\infty E_{u_iu_i}(f) cos 2\pi f t df \tag{56}$$

Frequency energy spectra are shown in Fig. 50.

Noting that $R_{u_iu_i}(t)$ is always symmetric if the flow is stationary, we have the integral time scale, T, and the micro time scale, $\tau_{u_iu_i}$, in the following relations:

$$T_{u_iu_i} = \frac{1}{u_i'^2}\int_0^\infty R_{u_iu_i}(t)dt = \frac{1}{4u_i'^2}\lim_{f\to 0} E_{u_iu_i}(f) \tag{57}$$

$$\frac{1}{(\tau_{u_iu_i})^2} = -\frac{1}{2u_i'^2}\left[\frac{\partial^2 R_{u_iu_i}(t)}{\partial t^2}\right]_{t=0} = \frac{2\pi^2}{u_i'^2}\int_0^\infty f^2 E_{u_iu_i}(f)df \; . \tag{58}$$

6.4.2 Taylor's hypothesis

It is possible to estimate wave number spectra from frequency spectra at which the assumption of 'frozen turbulence' is often used (see e.g. Frost [31]). If the velocity fluctuations, u, are much smaller than the convective velocity, U_{conv}, then a turbulent signal is thought of as if though it is just convected in time. Measurements at t and $t + \delta t$ can then be seen as measurements in space, a distance of $\delta t U_{conv}$ apart. This is the case if *Taylor's hypothesis* is true:

$$\frac{\partial}{\partial t} = -U_{conv}\frac{\partial}{\partial x} \; . \tag{59}$$

This is only approximately true, however, and only if the fluctuating velocity, u, is much smaller than the convecting velocity, U_{conv} (see Hinze [32]).

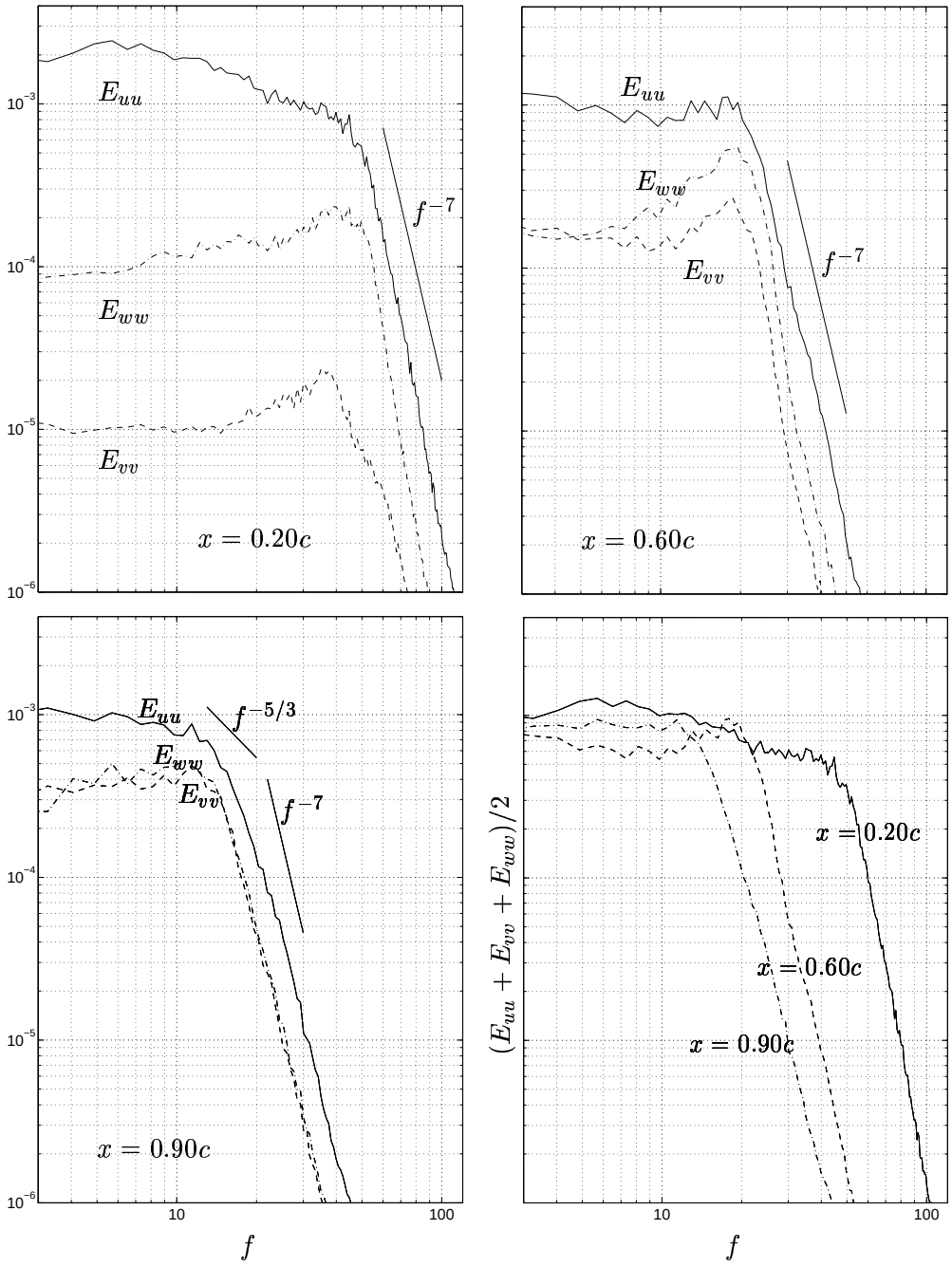

Figure 50: Frequency spectra of the resolved velocities at approximately 12% of the boundary layer.

With Taylor's hypothesis, the wave number k is related to the frequency, f, as $k = 2\pi f/U_{conv}$. We can then define the approximate wave

number spectrum from the frequency spectrum in Eq. 55 as

$$E_{u_iu_i}(k) = \frac{U_{conv}}{2\pi} E_{u_iu_i}(f) \ , \tag{60}$$

where the factor $U_{conv}/2\pi$ comes from the requirement that the integral over positive wave numbers of $E_{u_iu_i}(k)$ should be equal to $u_i'^2$. These spectra are in the streamwise direction.

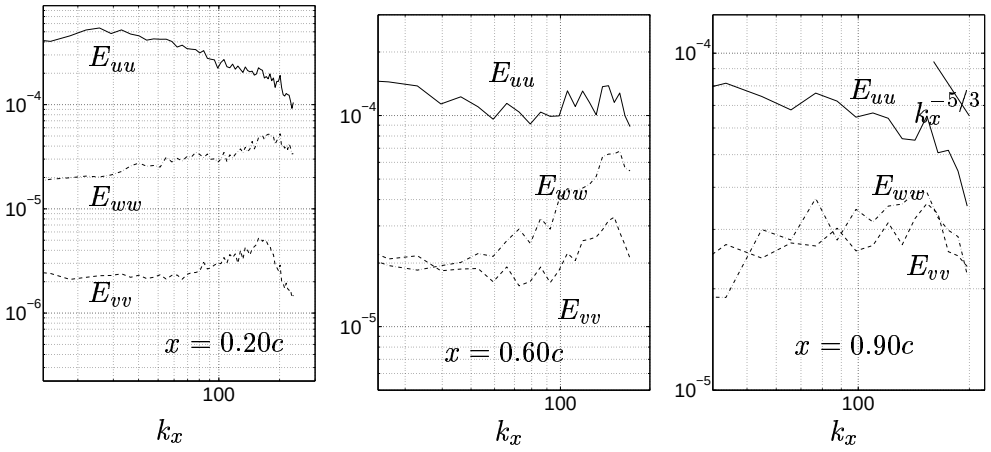

Figure 51: Approximate wave number spectra from the frequency spectra in Fig. 50 of the resolved velocities at $y/\delta \approx 0.12$.

The approximate wave number spectra obtained from the frequency spectra using Taylor's hypothesis are shown in Fig. 51. Here the spectra for wave numbers larger than $1/\Delta x$ have been rejected. The spatial resolution in the streamwise direction sets a limit on the highest frequencies for which the spectra are correct. This is seen in Fig. 50 as the steep slopes (as f^{-7}) at frequencies of approximately $\frac{U_{conv}}{2\pi\Delta x}$ (see Table 6). Note that the spectra in Fig. 50 could contain energy at frequencies that are larger than what is usually referred to as the highest frequency in turbulence, the Kolmogorov frequency $\tau^{-1} = (\nu/\epsilon)^{1/2}$. This is the highest frequency in a *Lagrangian viewpoint*, i.e. the highest frequency we would detect if we followed a fluid particle.

The other extreme, compared with the case in which Taylor's hypothesis is valid, is when there is turbulence with no mean convecting velocity. Then, the frequency, f, could be associated with wave numbers, k, by $f = u'k/(2\pi)$. Here, the turbulence intensity, u' (the velocity of the larger eddies), is seen as the convecting velocity for the smaller eddies (see Tennekes [33]). At the present points at $y/\delta \approx 0.12$, the ratios between the velocity fluctuations and the convecting mean velocity are approximately 14, 18 and 26 percent at x-locations $0.2c$, $0.6c$ and $0.9c$, respectively.

In isotropic turbulence, it can be shown (see e.g. Hinze [32]), that the transverse spectra in the inertial subrange are equal to four-thirds of the longitudinal spectrum, i.e

$$E_{ww} = E_{vv} = \frac{4}{3} E_{uu} \ , \text{ in the inertial subrange .} \tag{61}$$

The anisotropy in the resolved scales is seen at $x = 0.2c$ in Fig. 51, but, comparing the three figures, it is clearly seen that the turbulence becomes more isotropic in the downstream part of the boundary layer, especially between the transverse energy spectra (E_{ww} and E_{vv}) at $x = 0.9c$. It can be seen that the spectra reach more and more some sort of inertial subranges the more downstream in the boundary layer they are taken.

Returning to the spectra in the spanwise direction (Fig. 49), we also note the anisotropy in this direction. However, a larger extent of the presumed inertial subrange is covered in these spectra. This seems fair since the resolution in the spanwise direction is approximately twice as fine as the streamwise.

The estimated integral time scales from Eqs. 57 and the integral length scales ($L^x_{u_i u_i} \approx U_{conv} T^x_{u_i u_i}$) are shown in Table 9.

x/c	$T^x_{uu}c/U_\infty$	$T^x_{vv}c/U_\infty$	$T^x_{ww}c/U_\infty$	L^x_{uu}/c	L^x_{vv}/c	L^x_{ww}/c
0.20	$6.1 \cdot 10^{-3}$	$3.9 \cdot 10^{-3}$	$2.1 \cdot 10^{-3}$	$8.5 \cdot 10^{-3}$	$5.4 \cdot 10^{-3}$	$3.0 \cdot 10^{-3}$
0.60	$20 \cdot 10^{-3}$	$9.8 \cdot 10^{-3}$	$5.1 \cdot 10^{-3}$	$15 \cdot 10^{-3}$	$7.6 \cdot 10^{-3}$	$3.9 \cdot 10^{-3}$
0.90	$16 \cdot 10^{-3}$	$11 \cdot 10^{-3}$	$6.6 \cdot 10^{-3}$	$7.5 \cdot 10^{-3}$	$5.3 \cdot 10^{-3}$	$3.1 \cdot 10^{-3}$

Table 9: Longitudinal and transverse integral scales in the streamwise direction at $y/\delta \approx 0.12$.

In isotropic flow, the longitudinal integral length scale is twice the transverse length scale. By comparing the integral scales in the streamwise and spanwise directions, we see that there is no isotropy in the streamwise direction, but perhaps more isotropy in the other directions, especially at $x = 0.9c$.

Taylor's hypothesis can also be used to visualize the structures in an imaginary flow in a boundary layer over a flat plate with an unfavourable pressure gradient (see Figs. 52-54). The horisontal axis shows the signal in time scaled with the convective velocity, U_{conv}, and the vertical axis shows the signal in the spanwise direction (the scaling of the axes is the same). It is clearly seen how the spanwise structures become larger in the growing boundary layer. The relation between the integral scales can also be seen. Fig. 52 shows how the structures are very much elongated in the streamwise direction at 20% of the chord. This anisotropy decreases further downstream as Figs. 53 and 54 show.

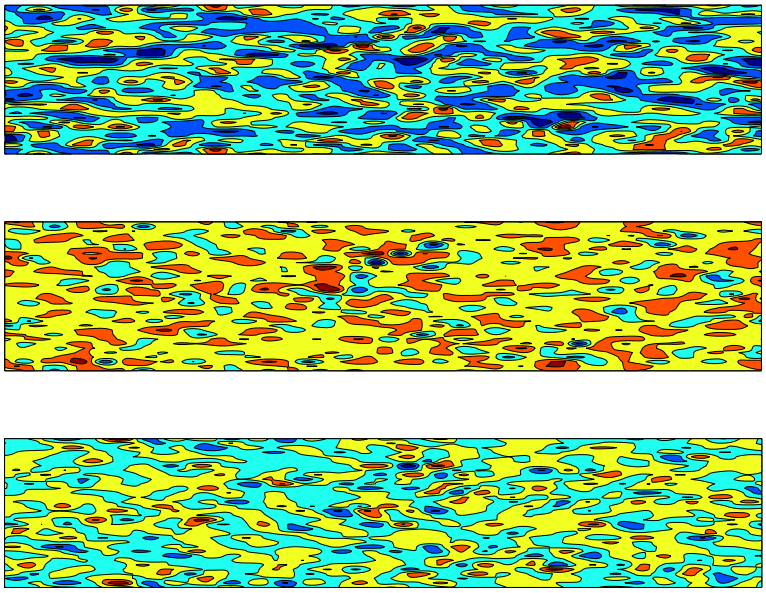

Figure 52: Spanwise and imaginary streamwise structures in space at $x = 0.2c$ and $y \approx 0.12c$. Contour plots of the resolved u-velocity (top figure), v-velocity and w-velocity (bottom figure).

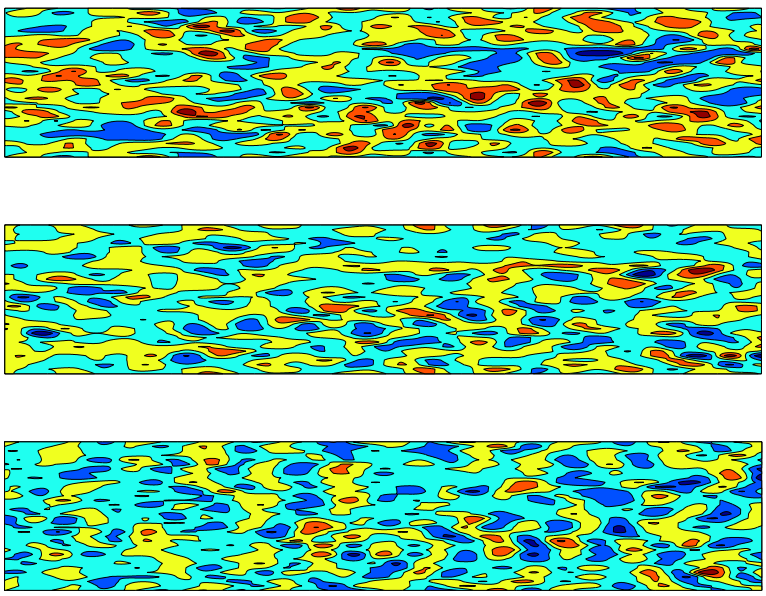

Figure 53: Spanwise and imaginary streamwise structures in space at $x = 0.6c$ and $y \approx 0.12c$. Contour plots of the resolved u-velocity (top figure), v-velocity and w-velocity (bottom figure).

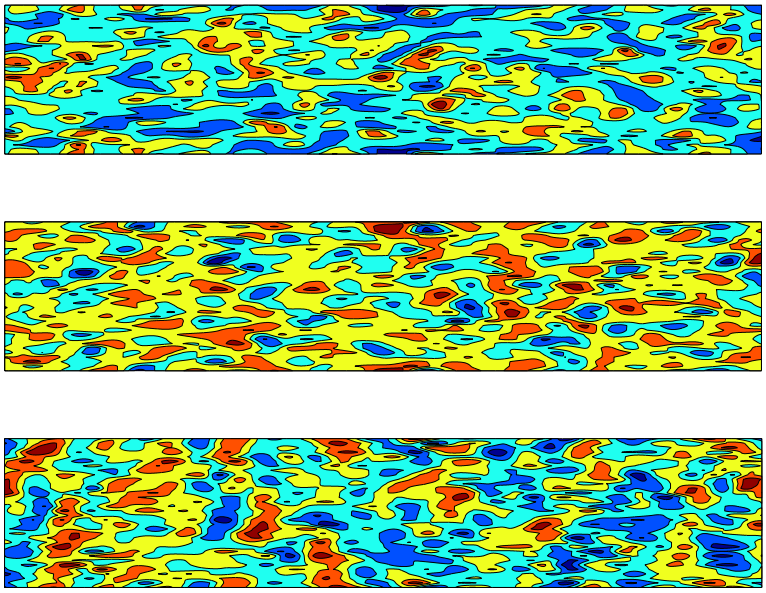

Figure 54: Spanwise and imaginary streamwise structures in space at $x = 0.9c$ and $y \approx 0.12c$. Contour plots of the resolved u-velocity (top figure), v-velocity and w-velocity (bottom figure).

6.5 Dissipation

It is interesting as to whether we can gain some information from these resolved spectra about the unresolved scales, for example, if we can estimate the dissipation, ϵ, and hence the smallest scales in turbulence, the Kolmogorov scales. As mentioned in the introduction, the main task of the SGS model is to dissipate the correct amount of energy from the resolved scales. The SGS model should model the small scales, the dissipative scales, and if the smallest resolved scales are in the Kolmogorov equilibrium range these scales might be locally isotropic. Thus it can be justifiable to use isotropic relations for SGS models, as is done e.g. with the Smagorinsky model.

From the microscales in Table 8, we can make a very crude estimate of the dissipation, ϵ. Assuming isotropic turbulence, the dissipation can be estimated as $\epsilon \approx 15\nu(\frac{(u')}{\lambda_z})^2$ (where u'^2 is taken as $k = \frac{1}{2}\overline{u_i u_i}$) and we arrive at an estimate of the Kolmogorov length scale too. Table 10 shows the very crude estimates of the dissipation compared with the SGS dissipation. The Kolmogorov length scale, η, and the microscale Reynolds number, $Re_\lambda = u'\lambda/\nu$, are also shown in the table.

The estimates of ϵ are used to plot the energy spectra in nondimensional form in Fig. 55 . Here the spanwise spectra has been cut off in a similar way as the streamwise spectra.

x/c	$-\epsilon_{sgs}\ [m^2 s^{-3}]$	$\epsilon\ [m^2 s^{-3}]$	η/c	Re_λ
0.20	0.85	0.38	$2.4 \cdot 10^{-5}$	350
0.60	$2.4 \cdot 10^{-2}$	0.12	$3.2 \cdot 10^{-5}$	300
0.90	$1.8 \cdot 10^{-3}$	$7.4 \cdot 10^{-2}$	$3.6 \cdot 10^{-5}$	290

Table 10: Estimates of the dissipation, the Kolmogorov length scale and the microscale Reynolds number at $y/\delta \approx 0.12$.

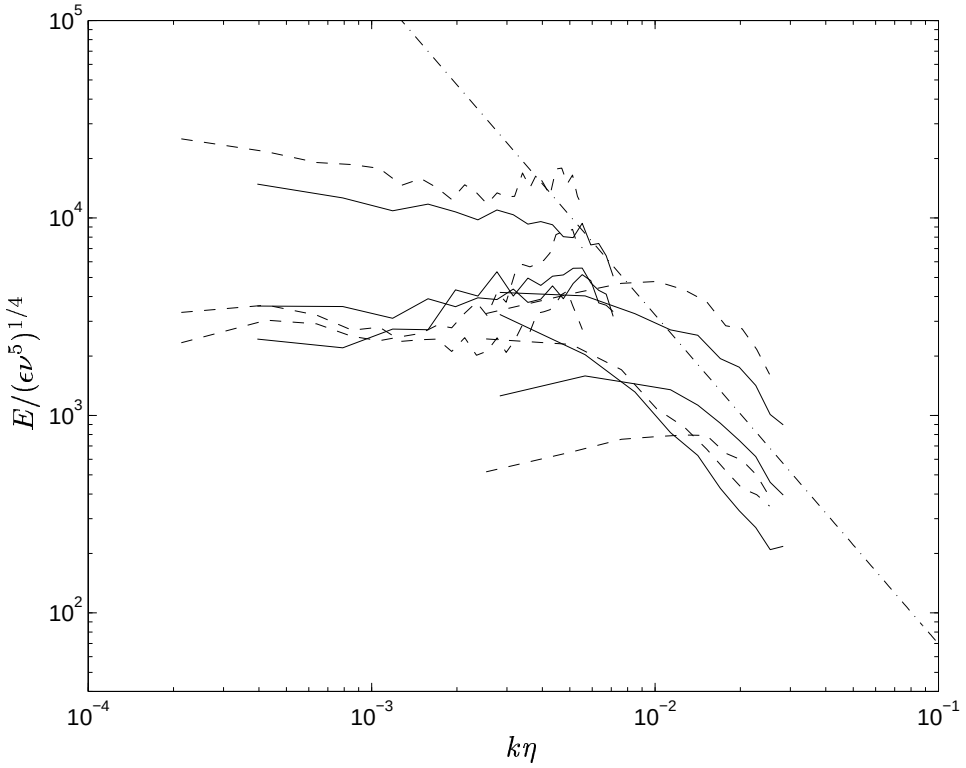

Figure 55: Dimensionless energy spectra at $x/c = 0.9$ (solid lines) and at $x/c = 0.6$ (dashed lines). The Kolmogorov $-5/3$ law with the Kolmogorov constant equal to 1.5 is also plotted.

6.6 Conclusions and Future Work

In this decelerating flow with curvature effects it is found that the resolution is in the order of the microscales. Somewhat downstream of the transition, at $x = 0.20c$, the resolved scales just barely reach an incipient inertial $-5/3$ range. A Δx^+ of 600 in this region is probably a little too coarse.

The energy spectra do not collapse in a universal scaling at high wave numbers as compared with Kolmogorov's universal scaling. How-

ever, the locations considered are fairly close to the wall and the scales are hence more anisotropic.

The anisotropy of the large scales is marked, especially just after the transition, with a far too energetic streamwise velocity and too little energy in the wall-normal direction. This striking anisotropy is probably not natural. See Chapter 4, where this is discussed. For example, it is found that the transition is not natural. It may be that some of the anisotropy seen in the spectra in the downstream part of the boundary layer is caused by the incorrectly prescribed transition.

In the near future, spectra will be computed from the simulation on the Common mesh (see Chapter 5) and compared with the other LES performed by the other partners in the LESFOIL project. In LES it is easy to collect data at a significant number of points in the boundary layer. For example, it would be interesting to study whether Kolmogorov's universal scaling is fulfilled in the outer parts of the boundary layer. Cospectra will also be studied. Further, a one-equation SGS model will be coupled with RANS in the near-wall region.

References

[1] L. Davidson. LESFOIL: an European project on large eddy simulations around a high-lift airfoil at high Reynolds number. In *ECCOMAS 2000, European Congress on Computational Methods in Applied Sciences and Engineering, 11-14 September*, Barcelona, Spain, 2000.

[2] EUROVAL- a European initiative on validation of CFD-codes. In W. Haase, F. Brandsma, E. Elsholz, M. Leschziner, and D. Schwamborn, editors, *Notes on Numerical Fluid Mechanics*, volume 42. Vieweg Verlag, 1993.

[3] ECARP- European Computational Aerodynamics Research Project: Validation of CFD Codes and Assessment of Turbulence Models. In W. Haase, E. Chaput, E. Elsholz, M. Leschziner, and U. Müller, editors, *Notes on Numerical Fluid Mechanics*, volume 58. Vieweg Verlag, 1997.

[4] L. Davidson and A. Rizzi. Navier-Stokes stall predictions using an algebraic stress model. *J. Spacecraft and Rockets*, 29:794–800, 1992.

[5] L. Davidson. Prediction of the flow around an airfoil using a Reynolds stress transport model. *ASME: Journal of Fluids Engineering*, 117:50–57, 1995.

[6] F.S. Lien and M.A. Leschziner. Modelling of 2D separation from high-lift aerofoils with a non-linear eddy-viscosity model and second-moment closure. *The Aeronautical Journal*, 99:125–144, 1995.

[7] S. Dahlström and L. Davidson. Large Eddy Simulation of the Flow around an Aerospatiale A-Aerofoil. In *ECCOMAS 2000, European Congress on Computational Methods in Applied Sciences and Engineering, 11-14 September*, Barcelona, Spain, 2000.

[8] M. Germano, U. Piomelli, P. Moin, and W.H. Cabot. A dynamic subgrid-scale eddy viscosity model. *Physics of Fluids A*, 3:1760–1765, 1991.

[9] P. Moin and J. Jimenez. Large eddy simulation of complex turbulent flows. 24th AIAA Fluid Dynamics Conference, AIAA Paper 93-3099, Orlando, 1993.

[10] U. Piomelli and J.R. Chasnov. Large-eddy simulations: Theory and applications. In D. Henningson, M. Hallbaeck, H. Alfreddson, and

A. Johansson, editors, *Transition and Turbulence Modelling*, pages 269–336, Dordrecht, 1996. Kluwer Academic Publishers.

[11] H. Tennekes and J.L. Lumley. *A First Course in Turbulence*. The MIT Press, Cambridge, Massachusetts, 1972.

[12] S.G. Saddoughi and S.V. Veeravalli. Local isotropy in turbulent boundary layers at high Reynolds number. *Journal of Fluid Mechanics*, 268:333–372, 1994.

[13] S.J. Kline, W.C. Reynolds, F.A. Schraub, and P.W. Runstadler. The structure of turbulent boundary layers. *Journal of Fluid Mechanics*, 30:741–773, 1967.

[14] P.R. Spalart, W-H. Jou, M. Strelets, and S.R. Allmaras. Comments on the feasibility of LES for wings, and on a hybrid RANS/LES approach. 1st AFOSR Int. Conf. on DNS/LES, Aug. 4-8, 1997, Ruston, LA. In *Advances in DNS/LES, C. Liu & Z. Liu Eds., Greyden Press, Columbus, OH*.

[15] L. Davidson. LES-RANS of channel flow. Technical Report 00/2, Dept. of Thermo and Fluid Dynamics, Chalmers University of Technology, Gothenburg, Sweden, 2000.

[16] L. Davidson and B. Farhanieh. CALC-BFC: A finite-volume code employing collocated variable arrangement and cartesian velocity components for computation of fluid flow and heat transfer in complex three-dimensional geometries. Rept. 92/4, Dept. of Thermo and Fluid Dynamics, Chalmers University of Technology, Gothenburg, 1992.

[17] C.M. Rhie and W.L. Chow. Numerical study of the turbulent flow past an airfoil with trailing edge separation. *AIAA Journal*, 21:1525–1532, 1983.

[18] H. Nilsson and L. Davidson. CALC-PVM: A parallel multiblock SIMPLE multiblock solver for turbulent flow in complex domains. Technical Report 98/12, Dept. of Thermo and Fluid Dynamics, Chalmers University of Technology, Gothenburg, 1998.

[19] T. Hellström and L. Davidson. A multiblock-moving mesh extension to the calc-bfc code. Rept. 93/3, Dept. of Thermo and Fluid Dynamics, Chalmers University of Technology, Gothenburg, 1993.

[20] J.H. Ferziger and M. Peric. *Computational Methods for Fluid Dynamics*. Springer-Verlag, Berlin, 1996.

[21] P.M. Gresho and R.L. Lee. Don't suppress the wiggles-they're telling you something! *Computers & Fluids*, 9:223–253, 1981.

[22] R.I. Issa. Solution of Implicitly Discretised Fluid Flow Equations by Operator-Splitting. *J. Comp. Physics*, 62:40–65, 1986.

[23] H.K. Versteeg and W. Malalasekera. *An Introduction to Computational Fluid Dynamics - The Finite Volume Method*. Longman Scientific & Technical, Harlow, England, 1995.

[24] T. Gough, S.Gao, P. Hancock, and P. R. Voke. Experiment and simulation of the tripped boundary layer on a flat plate: Comparative study. Technical Report ME-FD/95.40, Dept. of Mechanical Engineering, The University of Surrey, U.K., 1996.

[25] C. Mellen. Private communication. Institut für Hydrodynamik, University of Karlsruhe, Germany, 1999.

[26] S. Dahlström and L. Davidson. Chalmers' 12-months report, task 4, LESFOIL: A Brite-Euram project. Technical report, Dept. of Thermo and Fluid Dynamics, Chalmers University of Technology, Gothenburg, Sweden, 1999.

[27] C. Mellen, J. Fröhlich, and W. Rodi. Karlsruhe's 24-months report, task 5, LESFOIL: A Brite-Euram project. Technical report, Institut für Hydrodynamik, University of Karlsruhe, Germany, 2000.

[28] E. Chaput. Aerospatiale-A Airfoil. Contribution in ECARP- European Computational Aerodynamics Research Project: Validation of CFD Codes and Assessment of Turbulence Models. In W. Haase *et* al., editor, *Notes on Numerical Fluid Mechanics*, volume 58, pages 327–346. Vieweg Verlag, 1997.

[29] J.C. Le Balleur, P. Girodroux-Lavigne, and M. Néron. Viscous-Inviscid Interaction Methods in 2D/3D- Steady/Unsteady- Problems. Contribution by ONERA in ECARP- European Computational Aerodynamics Research Project: Validation of CFD Codes and Assessment of Turbulence Models. In W. Haase *et* al., editor, *Notes on Numerical Fluid Mechanics*, volume 58, pages 327–346. Vieweg Verlag, 1997.

[30] L.-E. Eriksson. G2DMESH, A 2D multi-block grid generator based on transfinite interpolation, User's guide.

[31] W. Frost. Spectral Theory of Turbulence. In W. Frost and T.H. Moulden, editors, *Handbook of Turbulence*, volume 1, pages 85–125, New York, 1977. Plenum Press.

[32] J.O. Hinze. *Turbulence*. McGraw-Hill, New York, second edition, 1975.

[33] H. Tennekes. Turbulence: Diffusion, Statistics, Spectral Dynamics. In W. Frost and T.H. Moulden, editors, *Handbook of Turbulence*, volume 1, pages 127–146, New York, 1977. Plenum Press.